Scilight

Intelligence & Control
https://www.sciltp.com/journals/ic



Check for updates

Article

Attack-Resilient Distributed Prescribed-Time Formation Control for Underactuated Unmanned Surface Vehicles Subject to Pose-Measurement False-Data Injection Attacks

Xiaohan Liu, Peichen Gong * and Jidong Liu

School of Computer Science and Artificial Intelligence, Shandong Normal University, Jinan 250358, China
* Correspondence: gongpeichen@126.com

How To Cite: Liu, X.; Gong, P.; Liu, J. Attack-Resilient Distributed Prescribed-Time Formation Control for Underactuated Unmanned Surface Vehicles Subject to Pose-Measurement False-Data Injection Attacks. *Intelligence & Control* **2026**, *2*(4), 3. https://doi.org/10.53941/ic.2026.100017

Received: 16 July 2026
Revised: 24 September 2026
Accepted: 10 October 2026
Published: 2 November 2026

Abstract: This paper investigates an attack-resilient distributed prescribed-time formation control problem for underactuated unmanned surface vehicles (USVs) subject to pose-measurement false-data injection (FDI) attacks, input saturation, external disturbances, collision-avoidance constraints, and connectivity-maintenance requirements. A secure-pose reconstruction layer is first developed to estimate the injected pose attack and remove its influence from the received position and yaw measurements. Based on the reconstructed pose, the distributed formation variables, prescribed-time transformed errors, virtual control laws, dynamic filters, disturbance observers, saturation auxiliary signals, adaptive laws, and actual surge-yaw inputs are redesigned. The residual propagation from pose-estimation errors to distance and bearing errors is explicitly characterized, and tightened prescribed-time performance boundaries are introduced to preserve the safety constraints for the true USV positions. Lyapunov analysis proves that the closed-loop error signals are uniformly ultimately bounded and that the prescribed-time formation-performance envelope is maintained under pose-measurement FDI attacks. Numerical simulations demonstrate that the proposed secure-pose compensation scheme improves formation tracking and safety performance compared with the uncompensated attack case.

Keywords: unmanned surface vehicles; false data injection attacks; prescribed-time control; formation control; input saturation; neural networks

1. Introduction

Unmanned surface vehicles (USVs) have attracted considerable attention in recent years owing to their broad applications in maritime surveillance, ocean resource exploration, environmental monitoring, search and rescue, and cooperative transportation [1–3]. Compared with a single USV, a coordinated fleet can improve mission efficiency, spatial coverage, fault tolerance, and operational flexibility in complex marine environments. Formation control is one of the fundamental problems in cooperative control, where multiple followers are required to track a leader or a prescribed reference trajectory while maintaining desired relative distances and bearing angles. Among various formation schemes, the leader-follower architecture is widely used because of its simple information structure, good scalability, and suitability for distributed implementation [4–7].

Despite these advantages, formation control of practical USVs remains challenging. First, most USVs are underactuated because direct actuation is unavailable in the sway direction, and the lateral motion has to be achieved through the coordination of surge and yaw dynamics [1, 8]. Second, the system dynamics usually contain hydrodynamic nonlinearities, unknown external disturbances, and actuator saturation. Third, due to limited sensing and communication capabilities, the relative distance among vehicles must satisfy collision-avoidance and connectivity-maintenance constraints. For these reasons, prescribed-time formation control has become an effective tool for USV cooperative systems [9–13]. By introducing a prescribed-time performance function and a suitable error transformation, relative-distance errors can be confined within a time-varying performance envelope, and the

Copyright: © 2026 by the authors. This is an open access article under the terms and conditions of the Creative Commons Attribution (CC BY) license (https://creativecommons.org/licenses/by/4.0/).
Publisher's Note: Scilight stays neutral with regard to jurisdictional claims in published maps and institutional affiliations.

convergence time can be specified a priori by the designer. A neural adaptive prescribed-time formation control method with input saturation was developed in [7], where nonlinear filters, predictors, neural approximators, and disturbance observers were integrated into a distributed backstepping framework.

Finite-time control guarantees convergence in a finite interval, but its settling time generally depends on the initial condition. Fixed-time control removes this dependence and provides a uniform settling-time upper bound, although that bound is normally determined indirectly by the controller parameters. In contrast, prescribed-time control allows the designer to assign the desired time before operation. In the present design, this advantage is combined with a time-varying performance envelope: the formation error is required to enter and thereafter remain within the designer-specified steady-state envelope no later than the prescribed time. This property is useful for coordinated maritime missions that require formation establishment or reconfiguration according to a predetermined schedule. The result should not be interpreted as exact zero-error convergence at the prescribed time; instead, it guarantees prescribed transient and steady-state error bounds.

However, most existing prescribed-time formation controllers are developed under the assumption that the exchanged pose information is reliable. This assumption may not hold in networked maritime cyber-physical systems, where false-data injection, replay, and stealthy attacks have been widely investigated [14–19]. Once the pose measurement or communication channel is compromised, an adversary may inject false data into the transmitted pose signal. In this case, the controller receives

$$\eta_{m,i}(t) = \eta_i(t) + a_i(t), \tag{1}$$

where $\eta_i(t)$ denotes the true pose of the ith USV and $a_i(t)$ denotes the injected false data. Different from matched input disturbances or actuator faults, pose-measurement FDI attacks directly corrupt the geometric information used to calculate leader-follower relative distances and bearing angles. Since these formation variables are nonlinear functions of position and yaw information, the injected attack does not enter the transformed formation error as a simple additive term. If the corrupted measurement $\eta_{m,i}(t)$ is directly used in a nominal prescribed-time controller, the logarithmic error transformation may lose its admissible domain, and the actual formation may violate collision-avoidance or connectivity constraints.

Cyberattack-resilient control has been studied for nonlinear multiagent systems under false-data injection attacks [20]. Nevertheless, directly applying those results to underactuated USV formation systems is nontrivial. The main difficulty lies in the coupling among pose attacks, nonlinear geometric formation errors, underactuated surge-yaw dynamics, input saturation, and prescribed-time safety constraints. In particular, even if an attack estimation error is bounded, its influence on the relative distance, bearing angle, auxiliary yaw angle, and transformed prescribed-time error must be explicitly quantified; otherwise, the safety guarantees for the true USV positions cannot be rigorously established.

Motivated by the above observations, this paper proposes an attack-resilient distributed prescribed-time formation control method for underactuated USVs subject to pose-measurement FDI attacks. The main idea is to incorporate an attack-estimation and secure-pose reconstruction layer before the distributed formation variables are generated. Based on the reconstructed secure pose, rather than the corrupted measurement, the prescribed-time formation-error generation and the complete distributed adaptive backstepping control design are reformulated.

The main contributions of this paper are summarized as follows.

(1) Unlike the nominal prescribed-time USV formation result in [7], this paper introduces pose-measurement FDI attacks into the leader–follower formation control problem of underactuated USVs. The effects of the injected attacks on the relative-distance, bearing-angle, and transformed prescribed-time errors are explicitly considered.

(2) A neural-network-based attack estimator is embedded into the distributed formation framework to reconstruct secure pose information. The residual effects of pose-estimation errors on the formation variables are bounded, and tightened prescribed-time performance constraints are designed to recover collision avoidance and connectivity maintenance for the true USV positions.

(3) Based on the reconstructed secure pose, a distributed adaptive backstepping controller is developed by integrating prescribed-time error transformation, dynamic filtering, prediction-based disturbance compensation, saturation handling, and surge-yaw input synthesis. The proposed design handles underactuation, unknown dynamics, external disturbances, input saturation, and pose-measurement FDI attacks in a unified framework.

(4) Lyapunov analysis proves that all closed-loop signals are uniformly ultimately bounded and that the prescribed-time formation tracking objective is achieved under pose-measurement FDI attacks while satisfying the required safety constraints.

The remainder of this paper is organized as follows. Section 2 presents the materials and methods, including

the communication topology, USV model, pose FDI attack model, secure-pose reconstruction mechanism, and distributed prescribed-time formation controller. Section 3 reports the theoretical and numerical results. Section 4 discusses the implications and limitations of the proposed method. Section 5 concludes this paper.

2. Materials and Methods

2.1. Notation and Communication Topology

Let $\mathbb{R}$, $\mathbb{R}_{>0}$, and $\mathbb{R}_{\geq 0}$ denote the sets of real numbers, positive real numbers, and nonnegative real numbers, respectively. For a vector x, $\|x\|$ denotes the Euclidean norm. For a real symmetric matrix P, $\lambda_{\min}(P)$ and $\lambda_{\max}(P)$ denote its minimum and maximum eigenvalues, respectively. The symbol I denotes an identity matrix with compatible dimension. The operator $\operatorname{atan2}(y, x)$ denotes the four-quadrant inverse tangent. The functions $\tanh(\cdot)$, $\cosh(\cdot)$, and $\operatorname{sech}(\cdot)$ are applied componentwise when their arguments are vectors.

The information exchange among USVs is described by a directed graph $\mathcal{G} = (\mathcal{V}, \mathcal{E})$, where $\mathcal{V} = \{0, 1, \ldots, N\}$ is the node set. Node 0 represents the virtual leader, and $\mathcal{F} = \{1, \ldots, N\}$ denotes the set of follower USVs. In this paper, the ordered pair $(i, j) \in \mathcal{E}$ means that follower i can receive information from node j, i.e., the information flows from j to i. The corresponding communication weight is denoted by a_{ij}, where $a_{ij} > 0$ if $(i, j) \in \mathcal{E}$, and $a_{ij} = 0$ otherwise. Self-loops are excluded, namely, $a_{ii} = 0$. The neighbor set of follower i is defined as

$$\mathcal{N}_i = \{j \in \mathcal{V} : a_{ij} > 0\}, \qquad i \in \mathcal{F}. \tag{2}$$

Furthermore, define

$$b_i = \sum_{j \in \mathcal{N}_i} a_{ij}, \qquad i \in \mathcal{F}. \tag{3}$$

Assumption 1 (Communication topology)**.** *The directed graph $\mathcal{G}$ contains a directed spanning tree rooted at the virtual leader. Equivalently, under the above information-flow convention, the virtual leader has an information path to every follower. Consequently, $b_i > 0$ holds for all $i \in \mathcal{F}$.*

2.2. Useful Lemmas

Lemma 1 (Young's inequality)**.** *For any $x, y \in \mathbb{R}^n$ and any $\epsilon > 0$,*

$$x^T y \leq \frac{\epsilon}{2}\|x\|^2 + \frac{1}{2\epsilon}\|y\|^2. \tag{4}$$

Lemma 2. *For any $z \in \mathbb{R}$ and any $\epsilon > 0$,*

$$0 \leq |z| - z \tanh\left(\frac{z}{\epsilon}\right) \leq \kappa_{\tanh}\epsilon, \tag{5}$$

where $\kappa_{\tanh} = 0.2785$.

2.3. Underactuated USV Model

Following the standard three-degree-of-freedom marine craft model [1,2,8], for the ith follower USV, $i \in \mathcal{F}$, the pose in the earth-fixed frame and the velocity in the body-fixed frame are denoted by

$$\bar{\eta}_i = [\bar{x}_i, \bar{y}_i, \psi_i]^T, \qquad \bar{\nu}_i = [u_i, \bar{v}_i, r_i]^T, \tag{6}$$

where $(\bar{x}_i, \bar{y}_i)$ is the position, ψ_i is the yaw angle, and u_i, $\bar{v}_i$, and r_i are the surge, sway, and yaw velocities, respectively. The kinematics are described by

$$\begin{aligned} \dot{\bar{x}}_i &= u_i \cos\psi_i - \bar{v}_i \sin\psi_i, \\ \dot{\bar{y}}_i &= u_i \sin\psi_i + \bar{v}_i \cos\psi_i, \\ \dot{\psi}_i &= r_i. \end{aligned} \tag{7}$$

The dynamics are given by

$$M_i \dot{\bar{\nu}}_i = -C_i(\bar{\nu}_i)\bar{\nu}_i - D_i(\bar{\nu}_i)\bar{\nu}_i + \operatorname{sat}(\tau_i) + D_{i,e}, \tag{8}$$

where M_i, $C_i(\bar{\nu}_i)$, and $D_i(\bar{\nu}_i)$ denote the inertia matrix, the Coriolis-centripetal matrix, and the damping matrix,

respectively, with

$$M_i = \begin{bmatrix} m_{i11} & 0 & 0 \\ 0 & m_{i22} & m_{i23} \\ 0 & m_{i32} & m_{i33} \end{bmatrix}, \tag{9}$$

$$C_i(\bar{\nu}_i) = \begin{bmatrix} 0 & 0 & c_{i13} \\ 0 & 0 & c_{i23} \\ c_{i31} & c_{i32} & 0 \end{bmatrix}, \tag{10}$$

and

$$D_i(\bar{\nu}_i) = \begin{bmatrix} d_{i11}(u_i) & 0 & 0 \\ 0 & d_{i22}(\bar{v}_i, r_i) & d_{i23}(\bar{v}_i, r_i) \\ 0 & d_{i32}(\bar{v}_i, r_i) & d_{i33}(\bar{v}_i, r_i) \end{bmatrix}. \tag{11}$$

The vector $D_{i,e} = [d_{i,u}, d_{i,v}, d_{i,r}]^T$ represents unknown environmental disturbances. Since the USV is underactuated, only the surge force and yaw moment are available, namely,

$$\mathrm{sat}(\tau_i) = [\mathrm{sat}(\tau_{i,u}), 0, \mathrm{sat}(\tau_{i,r})]^T. \tag{12}$$

For $h \in \{u, r\}$, the input saturation is described by

$$\mathrm{sat}(\tau_{i,h}) = \begin{cases} \tau_{i,h,\min}, & \tau_{i,h} \le \tau_{i,h,\min}, \\ \tau_{i,h}, & \tau_{i,h,\min} < \tau_{i,h} < \tau_{i,h,\max}, \\ \tau_{i,h,\max}, & \tau_{i,h} \ge \tau_{i,h,\max}, \end{cases} \tag{13}$$

where $\tau_{i,h,\min} < \tau_{i,h,\max}$ are known constants.

To facilitate the controller design for the underactuated dynamics, introduce the coordinate transformation

$$x_i = \bar{x}_i + \varepsilon_i \cos\psi_i, \quad y_i = \bar{y}_i + \varepsilon_i \sin\psi_i, \quad v_i = \bar{v}_i + \varepsilon_i r_i, \tag{14}$$

where $\varepsilon_i = m_{i23}/m_{i22}$. Let

$$\eta_i = [x_i, y_i, \psi_i]^T, \qquad \nu_i = [u_i, v_i, r_i]^T. \tag{15}$$

By differentiating (14) and using (7), the transformed kinematics can be obtained as

$$\begin{aligned} \dot{x}_i &= u_i \cos\psi_i - v_i \sin\psi_i, \\ \dot{y}_i &= u_i \sin\psi_i + v_i \cos\psi_i, \\ \dot{\psi}_i &= r_i. \end{aligned} \tag{16}$$

Furthermore, from (8), the compact transformed dynamics can be expressed as

$$\begin{aligned} \dot{u}_i &= \phi_{i,1}(\nu_i) + d_{i,1} + b_{i,1}\,\mathrm{sat}(\tau_{i,u}), \\ \dot{v}_i &= \phi_{i,2}(\nu_i) + d_{i,2}, \\ \dot{r}_i &= \phi_{i,3}(\nu_i) + d_{i,3} + b_{i,3}\,\mathrm{sat}(\tau_{i,r}), \end{aligned} \tag{17}$$

where $b_{i,1} = 1/m_{i11}$, $b_{i,3} = m_{i22}/\Delta_i$, and $\Delta_i = m_{i22}m_{i33} - m_{i23}m_{i32} > 0$. The functions $\phi_{i,q}(\nu_i)$, $q = 1, 2, 3$, collect the transformed hydrodynamic nonlinearities, and $d_{i,q}$ denote the transformed disturbances.

For the virtual leader, the reference pose is denoted by $\eta_0 = [x_0, y_0, \psi_0]^T$. It is assumed to be sufficiently smooth and to satisfy the same kinematic form as (16) with bounded virtual velocities u_0, v_0, and r_0.

Assumption 2 (Bounded disturbances and reference signals)**.** *For each $i \in \mathcal{F}$, the disturbances $d_{i,q}$, $q = 1, 2, 3$, and their first derivatives are bounded. The nonlinear functions $\phi_{i,q}(\nu_i)$ are continuous on a compact operating set. Moreover, the virtual leader signals η_0, u_0, v_0, r_0, and their required derivatives are bounded.*

2.4. Pose FDI Attack and Secure Pose Reconstruction

The transmitted pose measurement is assumed to be corrupted by an additive pose-measurement FDI attack:

$$\eta_{m,i}(t) = \eta_i(t) + a_i(t), \tag{18}$$

where $\eta_{m,i} = [\eta_{m,x,i}, \eta_{m,y,i}, \eta_{m,\psi,i}]^T$ is the received pose measurement, and $a_i = [a_{x,i}, a_{y,i}, a_{\psi,i}]^T$ is the injected false-data signal. For an attack-free vehicle, $a_i(t) \equiv 0$.

Assumption 3 (Pose FDI attack)**.** *For each $i \in \mathcal{F}$, $a_i(t)$ is continuously differentiable, and there exist constants $\bar{a}_i, \bar{a}_{d,i} > 0$ such that*

$$\|a_i(t)\| \le \bar{a}_i, \qquad \|\dot{a}_i(t)\| \le \bar{a}_{d,i}. \tag{19}$$

Remark 1. *Assumption 3 reflects both physical and analytical constraints. In practice, an injected signal is limited by sensor ranges, communication bandwidth, data formats, and the finite computation capability of the attacker; an excessively large or rapidly varying signal is also more readily detected by conventional anomaly monitors. Analytically, the bound on $\dot{a}_i$ is required to establish a bound on the residual derivative $\dot{n}_i$, which enters the reconstructed distance and bearing dynamics. The assumption covers smooth bias, drift, band-limited oscillatory, and smoothly windowed pulse attacks. Ideal jumps, impulsive attacks, and arbitrarily fast switching signals are outside the scope of the present analysis and require nonsmooth or hybrid-system tools.*

To estimate and compensate the injected signal, define

$$\vartheta_i(t) = \frac{k_{s,i}(t - t_0)}{k_{s,i}(t - t_0) + 1}, \qquad k_{s,i} > 0, \tag{20}$$

and construct the regressor

$$\zeta_{a,i} = [1, \vartheta_i, \eta_{m,i}^T, \nu_i^T]^T. \tag{21}$$

The neural-network-based attack estimator uses a fixed hidden layer and an online-adapted output layer, which avoids unnecessary nonlinear parameterization and permits direct reproduction. It is given by

$$\hat{a}_i = \bar{a} \odot \tanh\left(\hat{W}_{a,i}^T \sigma_a(V_a^T \zeta_{a,i}) \oslash \bar{a}\right), \tag{22}$$

where $V_a \in \mathbb{R}^{8 \times N_a}$ is a fixed hidden-layer matrix, $\hat{W}_{a,i} \in \mathbb{R}^{N_a \times 3}$ is the adaptive output-weight matrix, $\bar{a} = [4.5, 4.5, 0.55]^T$, and $\odot$ and $\oslash$ denote componentwise multiplication and division. The smooth output map enforces the attack-amplitude bounds. The auxiliary pose observer is designed as

$$\dot{\hat{\eta}}_i = J(\eta_{m,\psi,i} - \hat{a}_{\psi,i})\nu_i + L_i(\eta_{m,i} - \hat{\eta}_i - \hat{a}_i), \tag{23}$$

where $L_i = L_i^T > 0$ and

$$J(\psi) = \begin{bmatrix} \cos\psi & -\sin\psi & 0 \\ \sin\psi & \cos\psi & 0 \\ 0 & 0 & 1 \end{bmatrix}. \tag{24}$$

Let

$$e_{a,i} = \eta_{m,i} - \hat{\eta}_i - \hat{a}_i. \tag{25}$$

The output weights are updated by

$$\dot{\hat{W}}_{a,i} = \mathrm{Proj}\{\sigma_{a,i}(\Gamma_{W,a,i} e_{a,i})^T - \sigma_{W,i}\hat{W}_{a,i}\}, \tag{26}$$

where $\sigma_{a,i} = \sigma_a(V_a^T \zeta_{a,i})$, $\Gamma_{W,a,i} > 0$ is the learning-gain matrix, and $\sigma_{W,i} > 0$ is a leakage coefficient. The projection operator confines $\hat{W}_{a,i}$ to the Frobenius ball $\|\hat{W}_{a,i}\|_F \le W_{\max}$, as in standard robust adaptive control [21].

For implementation, $\zeta_{a,i} \in \mathbb{R}^8$, $N_a = 8$, $V_a = I_8$, and $\hat{W}_{a,i} \in \mathbb{R}^{8 \times 3}$. The componentwise hyperbolic-tangent activation

$$\sigma_a(z) = [\tanh(z_1), \ldots, \tanh(z_{N_a})]^T \tag{27}$$

is used. All implementation values, initial conditions, projection bounds, disturbance expressions, and numerical solver settings are collected in Table 1.

The secure pose used in the distributed formation controller is reconstructed as

$$\eta_i^s = \eta_{m,i} - \hat{a}_i = \eta_i + n_i, \tag{28}$$

where $n_i = a_i - \hat{a}_i$ is the attack-estimation residual. Denote

$$p_i^s = P\eta_i^s = [x_i^s, y_i^s]^T, \qquad \psi_i^s = e_3^T \eta_i^s, \tag{29}$$

where $P = [I_2\ 0_{2\times 1}]$ and $e_3 = [0, 0, 1]^T$.

Table 1. Implementation and numerical-integration settings.

Item	Value Used in the Numerical Study
Activation function	$\sigma_a(z) = [\tanh(z_1), \ldots, \tanh(z_{N_a})]^T$
Hidden neurons N_a	8
Fixed hidden weights	$V_a = I_8$
Observer gain L_i	$\mathrm{diag}\{2.2, 2.2, 1.6\}$
Scheduling gain $k_{s,i}$	0.40
Learning and leakage gains	$\Gamma_{W,a,i} = \mathrm{diag}\{8.0, 8.0, 5.2\}$; $\sigma_{W,i} = 0.02$
Initial observer state	$\hat{\eta}_i(0) = \eta_i(0)$
Initial adaptive weights	$\hat{W}_{a,i}(0) = 0_{8\times 3}$
Weight projection set	$\|\hat{W}_{a,i}\|_F \le 12$
Attack-output bounds	$[4.5, 4.5, 0.55]^T$
Disturbances	$d_{i,u} = 0.030\sin(0.17t + 0.40i) + 0.018\cos(0.07t)$; $d_{i,v} = 0.020\cos(0.13t + 0.25i)$; $d_{i,r} = 0.025\sin(0.19t + 0.30i)$
Numerical solver	MATLAB R2022a, ode45
Solver tolerances	RelTol $= 10^{-6}$, AbsTol $= 10^{-8}$, MaxStep $= 0.05$ s
Other initial states	$\nu_i(0) = 0$; all adaptive output weights are zero
Simulation interval	$[0, 120]$ s

Lemma 3. *Suppose that $\zeta_{a,i}$ and $\dot{\zeta}_{a,i}$ are bounded on the compact operating set. Under Assumption 3 and the projection-based update law (26), n_i and $\dot{n}_i$ are bounded. Hence, there exist finite constants $\bar{n}_{p,i}, \bar{n}_{\psi,i}, \bar{n}_{d,i} > 0$ such that*

$$\|Pn_i\| \le \bar{n}_{p,i}, \quad |e_3^T n_i| \le \bar{n}_{\psi,i}, \quad \|\dot{n}_i\| \le \bar{n}_{d,i}. \tag{30}$$

Proof. By the projection property, $\hat{W}_{a,i}$ is confined to a compact set. Since V_a is fixed and $\zeta_{a,i}$, $\dot{\zeta}_{a,i}$, $\sigma_a(\cdot)$, and $\sigma_a'(\cdot)$ are bounded on the compact operating set, $\hat{a}_i$ and $\dot{\hat{a}}_i$ are bounded. Together with the boundedness of a_i and $\dot{a}_i$ in Assumption 3, this implies that $n_i = a_i - \hat{a}_i$ and $\dot{n}_i = \dot{a}_i - \dot{\hat{a}}_i$ are bounded. Therefore, the bounds in (30) hold. □

2.5. Formation Objective

For each communication edge $(i, j) \in \mathcal{E}$, define the true relative position, distance, and bearing angle as

$$p_{ij} = p_j - p_i, \qquad l_{ij} = \|p_{ij}\|, \tag{31}$$

and

$$\theta_{ij} = \mathrm{atan2}(y_j - y_i, x_j - x_i), \tag{32}$$

where $p_i = [x_i, y_i]^T$. The desired relative distance and bearing angle are denoted by $l_{ij,d}$ and $\theta_{ij,d}$, respectively. The desired distance is selected inside the admissible safety interval, i.e.,

$$l_{ij,\mathrm{col}} < l_{ij,d} < l_{ij,\mathrm{con}}, \tag{33}$$

where $l_{ij,\mathrm{col}} > 0$ and $l_{ij,\mathrm{con}} > l_{ij,\mathrm{col}}$ denote the prescribed collision-avoidance distance and maximum communication distance, respectively. The true inter-USV distance is required to satisfy

$$l_{ij,\mathrm{col}} < l_{ij}(t) < l_{ij,\mathrm{con}}. \tag{34}$$

The objective of this paper is to design distributed surge-yaw control inputs $\tau_{i,u}$ and $\tau_{i,r}$, $i \in \mathcal{F}$, such that, under the pose FDI attack (18), all closed-loop signals are bounded, the followers track the virtual leader while maintaining the desired formation, and the true distance constraint (34) is preserved. The prescribed-time performance function and the corresponding transformed formation errors are introduced in the next section.

2.6. Distributed Secure Prescribed-Time Formation Design

2.6.1. Secure Distance and Bearing Dynamics

Based on the reconstructed secure pose η_i^s, define the relative position, distance, bearing angle, and distance error associated with edge $(i,j) \in \mathcal{E}$ as

$$p_{ij}^s = p_j^s - p_i^s, \qquad l_{ij}^s = \|p_{ij}^s\|, \tag{35}$$

$$\theta_{ij}^s = \operatorname{atan2}(y_j^s - y_i^s, x_j^s - x_i^s), \tag{36}$$

and

$$z_{ij}^s = l_{ij}^s - l_{ij,d}. \tag{37}$$

Let $X_i = [u_i, v_i]^T$ and

$$R(\psi_i^s) = \begin{bmatrix} \cos\psi_i^s & -\sin\psi_i^s \\ \sin\psi_i^s & \cos\psi_i^s \end{bmatrix}. \tag{38}$$

Since $\eta_i^s = \eta_i + n_i$, the secure position and yaw dynamics can be written as

$$\dot{p}_i^s = R(\psi_i^s)X_i + d_{p,i}^a, \qquad \dot{\psi}_i^s = r_i + d_{\psi,i}^a, \tag{39}$$

where

$$d_{p,i}^a = [R(\psi_i) - R(\psi_i^s)]X_i + P\dot{n}_i, \tag{40}$$

and

$$d_{\psi,i}^a = e_3^T \dot{n}_i. \tag{41}$$

By Lemma 3 and the compactness of the operating set, $d_{p,i}^a$ and $d_{\psi,i}^a$ are bounded.

For subsequent use, define

$$\delta_{l,ij}^a = [\cos\theta_{ij}^s, \sin\theta_{ij}^s](d_{p,j}^a - d_{p,i}^a), \tag{42}$$

and

$$\delta_{\theta,ij}^a = \frac{[-\sin\theta_{ij}^s, \cos\theta_{ij}^s](d_{p,j}^a - d_{p,i}^a)}{l_{ij}^s}. \tag{43}$$

Differentiating l_{ij}^s and θ_{ij}^s along (39) gives

$$\begin{aligned} \dot{l}_{ij}^s = &-u_i\cos(\psi_i^s - \theta_{ij}^s) + u_j\cos(\psi_j^s - \theta_{ij}^s) \\ &+ v_i\sin(\psi_i^s - \theta_{ij}^s) - v_j\sin(\psi_j^s - \theta_{ij}^s) + \delta_{l,ij}^a, \end{aligned} \tag{44}$$

and

$$\begin{aligned} \dot{\theta}_{ij}^s = &\frac{1}{l_{ij}^s}[-u_i\sin(\psi_i^s - \theta_{ij}^s) + u_j\sin(\psi_j^s - \theta_{ij}^s) \\ &- v_i\cos(\psi_i^s - \theta_{ij}^s) + v_j\cos(\psi_j^s - \theta_{ij}^s)] + \delta_{\theta,ij}^a. \end{aligned} \tag{45}$$

The above equations show explicitly how the attack-estimation residual enters the secure formation dynamics.

2.6.2. Prescribed-Time Error Transformation

Choose the prescribed-time tuning function as

$$\rho_i(t) = \begin{cases} (\rho_{i,0} - \rho_{i,\infty})\sin^2\left(\dfrac{\pi(T_i - t)}{2T_i}\right) + \rho_{i,\infty}, & t < T_i, \\ \rho_{i,\infty}, & t \geq T_i, \end{cases} \tag{46}$$

where $T_i > 0$ is the prescribed time, $\rho_{i,0} > \rho_{i,\infty} > 0$ is the initial performance level, and $\rho_{i,\infty}$ is the steady-state performance level. Thus, $\rho_i(0) = \rho_{i,0}$ and $\rho_i(t) = \rho_{i,\infty}$ for $t \geq T_i$. Let $\kappa_{ij}^s > 0$ be a tightened performance boundary. The transformed secure distance error is designed as

$$\xi_{ij}^s = \ln\frac{\kappa_{ij}^s\rho_i + z_{ij}^s}{\kappa_{ij}^s\rho_i - z_{ij}^s}. \tag{47}$$

The transformation is well defined if

$$|z_{ij}^s| < \kappa_{ij}^s \rho_i. \tag{48}$$

Define

$$\Pi_{ij}^s = \frac{2\kappa_{ij}^s \rho_i}{(\kappa_{ij}^s)^2 \rho_i^2 - (z_{ij}^s)^2}. \tag{49}$$

Then differentiating (47) yields

$$\dot{\xi}_{ij}^s = \Pi_{ij}^s \left(\dot{l}_{ij}^s - \frac{\dot{\rho}_i}{\rho_i} z_{ij}^s \right). \tag{50}$$

The secure kinematic formation errors are selected as

$$\begin{aligned} s_{i,11} &= \sum_{j \in \mathcal{N}_i} a_{ij} \xi_{ij}^s, \\ s_{i,12} &= \sum_{j \in \mathcal{N}_i} a_{ij} (\theta_{ij}^s - \theta_{ij,d}), \\ s_{i,13} &= \sum_{j \in \mathcal{N}_i} a_{ij} (\psi_i^s - \psi_{ij,a}^s). \end{aligned} \tag{51}$$

The auxiliary yaw angle is defined by

$$\psi_{ij,a}^s = [\operatorname{atan2}(h_{ij,1}^s, h_{ij,2}^s) - \psi_j^s] \tanh(h_{ij,3}^s) + \psi_j^s, \tag{52}$$

where

$$\begin{aligned} h_{ij,1}^s &= l_{ij}^s \sin\theta_{ij}^s - l_{ij,d} \sin\theta_{ij,d}, \\ h_{ij,2}^s &= l_{ij}^s \cos\theta_{ij}^s - l_{ij,d} \cos\theta_{ij,d}, \\ h_{ij,3}^s &= c_{ij}[(l_{ij}^s - l_{ij,d})^2 + (\theta_{ij}^s - \theta_{ij,d})^2], \end{aligned} \tag{53}$$

with $c_{ij} > 0$. This auxiliary angle follows the leader-neighbor yaw when the formation error is small and avoids a singular heading command when the relative-distance and bearing errors approach zero.

Let

$$S_{i,1} = [s_{i,11}, s_{i,12}]^T, \qquad S_{i,2} = [s_{i,21}, s_{i,22}]^T. \tag{54}$$

Substituting (44)–(50) into (51) yields

$$\dot{S}_{i,1} = -H_{i,1}^s X_i + H_{i,2}^s - D_i^s + \Delta_i^a, \tag{55}$$

where $c_{k,ij}^s = \cos(\psi_k^s - \theta_{ij}^s)$ and $s_{k,ij}^s = \sin(\psi_k^s - \theta_{ij}^s)$ for $k = i, j$, and

$$H_{i,1}^s = \sum_{j \in \mathcal{N}_i} a_{ij} \begin{bmatrix} \Pi_{ij}^s c_{i,ij}^s & -\Pi_{ij}^s s_{i,ij}^s \\ s_{i,ij}^s / l_{ij}^s & c_{i,ij}^s / l_{ij}^s \end{bmatrix}, \tag{56}$$

$$H_{i,2}^s = \sum_{j \in \mathcal{N}_i} a_{ij} \begin{bmatrix} \Pi_{ij}^s c_{j,ij}^s & -\Pi_{ij}^s s_{j,ij}^s \\ s_{j,ij}^s / l_{ij}^s & c_{j,ij}^s / l_{ij}^s \end{bmatrix} \begin{bmatrix} u_j \\ v_j \end{bmatrix}, \tag{57}$$

$$D_i^s = \sum_{j \in \mathcal{N}_i} a_{ij} \begin{bmatrix} \Pi_{ij}^s \dfrac{\dot{\rho}_i}{\rho_i} z_{ij}^s \\ 0 \end{bmatrix}, \tag{58}$$

and

$$\Delta_i^a = \sum_{j \in \mathcal{N}_i} a_{ij} \begin{bmatrix} \Pi_{ij}^s \delta_{l,ij}^a \\ \delta_{\theta,ij}^a \end{bmatrix}. \tag{59}$$

Furthermore, the derivative of $s_{i,13}$ satisfies

$$\dot{s}_{i,13} = b_i r_i - \varpi_i^s + \Delta_{i,\psi}^a, \tag{60}$$

where b_i is defined in (3), and

$$\varpi_i^s = \sum_{j \in \mathcal{N}_i} a_{ij} \dot{\psi}_{ij,a}^s, \qquad \Delta_{i,\psi}^a = b_i d_{\psi,i}^a. \tag{61}$$

Assumption 4 (Nonsingularity of the formation matrix)**.** *The matrix $H_{i,1}^s$ is nonsingular on the compact operating set, and there exists a constant $\bar{H}_i > 0$ such that*

$$\|H_{i,1}^s\| \le \bar{H}_i, \qquad \|(H_{i,1}^s)^{-1}\| \le \bar{H}_i. \tag{62}$$

2.6.3. Residual Bounds and Tightened Boundary

Define

$$\bar{\delta}_{ij} = \bar{n}_{p,i} + \bar{n}_{p,j}. \tag{63}$$

Since $p_{ij}^s = p_{ij} + P(n_j - n_i)$, it follows from Lemma 3 that

$$|l_{ij}^s - l_{ij}| \le \bar{\delta}_{ij}. \tag{64}$$

If $l_{ij} \ge l_{\min,ij} > 0$ and $\bar{\delta}_{ij} < l_{\min,ij}/2$, then the bearing-angle residual satisfies

$$|\theta_{ij}^s - \theta_{ij}| \le \arcsin \frac{\bar{\delta}_{ij}}{l_{\min,ij} - \bar{\delta}_{ij}}. \tag{65}$$

To guarantee the true distance constraint in (34), the tightened boundary is selected to satisfy

$$\kappa_{ij}^s + \bar{\delta}_{ij} < \min\{l_{ij,d} - l_{ij,\mathrm{col}}, l_{ij,\mathrm{con}} - l_{ij,d}\}. \tag{66}$$

Indeed, (48) and $0 < \rho_i(t) \le 1$ imply

$$l_{ij,d} - \kappa_{ij}^s < l_{ij}^s(t) < l_{ij,d} + \kappa_{ij}^s. \tag{67}$$

Combining this inequality with (64) and (66) gives (34). Thus, the tightened prescribed-time boundary compensates for the possible distance mismatch caused by attack-estimation residuals.

2.6.4. Virtual Control and Nonlinear Filters

Define

$$f_i = H_{i,1}^{sT} S_{i,1} = [f_{i,1}, f_{i,2}]^T, \tag{68}$$

and

$$\Theta_i = \begin{bmatrix} \tanh(f_{i,1}/\bar{\sigma}_{i,1}) \\ \tanh(f_{i,2}/\bar{\sigma}_{i,2}) \end{bmatrix}, \qquad \Theta_{i,3} = \tanh(b_i s_{i,13}/\bar{\sigma}_{i,3}), \tag{69}$$

where $\bar{\sigma}_{i,q} > 0$. The virtual controls are designed as

$$\alpha_i = (H_{i,1}^s)^{-1}(K_{i,1} S_{i,1} + H_{i,2}^s - D_i^s) + \Theta_i, \tag{70}$$

and

$$\alpha_{i,3} = \frac{-k_{i,13} s_{i,13} + \varpi_i^s}{b_i} - \Theta_{i,3}, \tag{71}$$

where $K_{i,1} = \mathrm{diag}\{k_{i,11}, k_{i,12}\} > 0$ and $k_{i,13} > 0$.

To avoid repeated differentiation of virtual controls, introduce the nonlinear filters following the dynamic-surface-control idea [22]

$$\begin{cases} \iota_{i,q} \dot{\bar{\alpha}}_{i,q} = -\tilde{\alpha}_{i,q} - \iota_{i,q} \hat{\chi}_{i,q} \tanh\left(\dfrac{\hat{\chi}_{i,q} \tilde{\alpha}_{i,q}}{\sigma_{i,q}}\right), \\ \bar{\alpha}_{i,q}(0) = \alpha_{i,q}(0), \end{cases} \tag{72}$$

where

$$\tilde{\alpha}_{i,q} = \bar{\alpha}_{i,q} - \alpha_{i,q}, \qquad q = 1, 2, 3. \tag{73}$$

The adaptive law for $\hat{\chi}_{i,q}$ is

$$\dot{\hat{\chi}}_{i,q} = \iota_{i,q} |\tilde{\alpha}_{i,q}| - \ell_{i,q} \hat{\chi}_{i,q}, \tag{74}$$

where $\iota_{i,q}$, $\ell_{i,q}$, and $\sigma_{i,q}$ are positive design constants. Define the dynamic surface errors as

$$\begin{aligned} s_{i,21} &= u_i - \bar{\alpha}_{i,1} - \tanh(\beta_{i,1}), \\ s_{i,22} &= v_i - \bar{\alpha}_{i,2} - \tanh(\beta_{i,2}), \\ s_{i,23} &= r_i - \bar{\alpha}_{i,3} - \tanh(\beta_{i,3}). \end{aligned} \tag{75}$$

2.6.5. Surface-Error Predictors and Disturbance Observers

For $q = 1, 2, 3$, the unknown nonlinear term is approximated by neural-network basis functions [23–26]

$$\phi_{i,q}(\nu_i) = \theta_{i,q}^{*T}\varphi_{i,q}(\nu_i) + \epsilon_{i,q}(\nu_i), \tag{76}$$

where $\theta_{i,q}^*$ is an ideal constant weight vector, $\varphi_{i,q}$ is a bounded basis vector, and $|\epsilon_{i,q}| \le \bar{\epsilon}_{i,q}$. Define the generalized disturbance

$$D_{i,q} = d_{i,q} + \epsilon_{i,q}. \tag{77}$$

Let

$$\Omega_{i,q} = \frac{\varphi_{i,q}^T\varphi_{i,q}}{4\gamma_{i,q}^2}, \qquad \vartheta_{i,q} = -\|\theta_{i,q}^*\|^2, \tag{78}$$

where $\gamma_{i,q} > 0$. The predictor error is defined as

$$\tilde{s}_{i,2q} = \hat{s}_{i,2q} - s_{i,2q}. \tag{79}$$

The surface-error predictors are designed as

$$\begin{aligned} \dot{\hat{s}}_{i,21} = {} & \hat{\vartheta}_{i,1}\Omega_{i,1}\tilde{s}_{i,21} + \hat{D}_{i,1} + b_{i,1}\,\mathrm{sat}(\tau_{i,u}) + \frac{1}{\iota_{i,1}}\tilde{\alpha}_{i,1} \\ & - \mathrm{sech}^2(\beta_{i,1})\dot{\beta}_{i,1} + \hat{\chi}_{i,1}\tanh\left(\frac{\hat{\chi}_{i,1}\tilde{\alpha}_{i,1}}{\sigma_{i,1}}\right) \\ & - (c_{i,1} + c_{i,e1})\tilde{s}_{i,21} - f_{i,1}, \end{aligned} \tag{80}$$

$$\begin{aligned} \dot{\hat{s}}_{i,22} = {} & \hat{\vartheta}_{i,2}\Omega_{i,2}\tilde{s}_{i,22} + \hat{D}_{i,2} + \frac{1}{\iota_{i,2}}\tilde{\alpha}_{i,2} - \mathrm{sech}^2(\beta_{i,2})\dot{\beta}_{i,2} \\ & + \hat{\chi}_{i,2}\tanh\left(\frac{\hat{\chi}_{i,2}\tilde{\alpha}_{i,2}}{\sigma_{i,2}}\right) - (c_{i,2} + c_{i,e2})\tilde{s}_{i,22} - f_{i,2}, \end{aligned} \tag{81}$$

and

$$\begin{aligned} \dot{\hat{s}}_{i,23} = {} & \hat{\vartheta}_{i,3}\Omega_{i,3}\tilde{s}_{i,23} + \hat{D}_{i,3} + b_{i,3}\,\mathrm{sat}(\tau_{i,r}) + \frac{1}{\iota_{i,3}}\tilde{\alpha}_{i,3} \\ & - \mathrm{sech}^2(\beta_{i,3})\dot{\beta}_{i,3} + \hat{\chi}_{i,3}\tanh\left(\frac{\hat{\chi}_{i,3}\tilde{\alpha}_{i,3}}{\sigma_{i,3}}\right) \\ & - (c_{i,3} + c_{i,e3})\tilde{s}_{i,23} + b_i s_{i,13}. \end{aligned} \tag{82}$$

The predictor-based disturbance observers are constructed as [27].

$$\hat{D}_{i,q} = c_{i,dq}(\hat{s}_{i,2q} - \hat{\omega}_{i,q}), \tag{83}$$

where

$$\begin{aligned} \dot{\hat{\omega}}_{i,1} = {} & \hat{\vartheta}_{i,1}\Omega_{i,1}\tilde{s}_{i,21} + b_{i,1}\,\mathrm{sat}(\tau_{i,u}) + c_{i,D1}\hat{D}_{i,1} + \frac{1}{\iota_{i,1}}\tilde{\alpha}_{i,1} \\ & - \mathrm{sech}^2(\beta_{i,1})\dot{\beta}_{i,1} + \hat{\chi}_{i,1}\tanh\left(\frac{\hat{\chi}_{i,1}\tilde{\alpha}_{i,1}}{\sigma_{i,1}}\right) \\ & + (c_{i,d1}^{-1} - (c_{i,1} + c_{i,e1}))\tilde{s}_{i,21} - f_{i,1}, \end{aligned} \tag{84}$$

$$\begin{aligned} \dot{\hat{\omega}}_{i,2} = {} & \hat{\vartheta}_{i,2}\Omega_{i,2}\tilde{s}_{i,22} + c_{i,D2}\hat{D}_{i,2} + \frac{1}{\iota_{i,2}}\tilde{\alpha}_{i,2} - \mathrm{sech}^2(\beta_{i,2})\dot{\beta}_{i,2} \\ & + \hat{\chi}_{i,2}\tanh\left(\frac{\hat{\chi}_{i,2}\tilde{\alpha}_{i,2}}{\sigma_{i,2}}\right) \\ & + (c_{i,d2}^{-1} - (c_{i,2} + c_{i,e2}))\tilde{s}_{i,22} - f_{i,2}, \end{aligned} \tag{85}$$

and

$$\begin{aligned}\dot{\hat{\omega}}_{i,3} = {} & \hat{\vartheta}_{i,3}\Omega_{i,3}\tilde{s}_{i,23} + b_{i,3}\,\mathrm{sat}(\tau_{i,r}) + c_{i,D3}\hat{D}_{i,3} + \frac{1}{\iota_{i,3}}\tilde{\alpha}_{i,3} \\ & - \mathrm{sech}^2(\beta_{i,3})\dot{\beta}_{i,3} + \hat{\chi}_{i,3}\tanh\left(\frac{\hat{\chi}_{i,3}\tilde{\alpha}_{i,3}}{\sigma_{i,3}}\right) \\ & + (c_{i,d3}^{-1} - (c_{i,3} + c_{i,e3}))\tilde{s}_{i,23} + b_i s_{i,13}.\end{aligned} \tag{86}$$

The adaptive law for $\hat{\vartheta}_{i,q}$ is

$$\dot{\hat{\vartheta}}_{i,q} = \Gamma_{i,q}\left(-\Omega_{i,q}\tilde{s}_{i,2q}^2 - \lambda_{i,q}\hat{\vartheta}_{i,q}\right), \tag{87}$$

where $\Gamma_{i,q} > 0$ and $\lambda_{i,q} > 0$.

2.6.6. Saturation Auxiliary Signals and Actual Inputs

The auxiliary variables used to compensate input saturation and underactuation are designed as

$$\dot{\beta}_{i,1} = \cosh^2(\beta_{i,1})[-\mu_{i,1}\beta_{i,1} - b_{i,1}(\tau_{i,u} - \mathrm{sat}(\tau_{i,u}))], \tag{88}$$

$$\begin{aligned}\dot{\beta}_{i,2} = {} & \cosh^2(\beta_{i,2})[\hat{\vartheta}_{i,2}\Omega_{i,2}\tilde{s}_{i,22} + c_{i,2}s_{i,22} + \frac{1}{\iota_{i,2}}\tilde{\alpha}_{i,2} \\ & + \hat{\chi}_{i,2}\tanh\left(\frac{\hat{\chi}_{i,2}\tilde{\alpha}_{i,2}}{\sigma_{i,2}}\right) + \hat{D}_{i,2} - 2f_{i,2}],\end{aligned} \tag{89}$$

and

$$\dot{\beta}_{i,3} = \cosh^2(\beta_{i,3})[-\mu_{i,3}\beta_{i,3} - b_{i,3}(\tau_{i,r} - \mathrm{sat}(\tau_{i,r}))], \tag{90}$$

where $\mu_{i,1}, \mu_{i,3} > 0$. The actual control inputs are given by

$$\begin{aligned}\tau_{i,u} = {} & b_{i,1}^{-1}[-\hat{\vartheta}_{i,1}\Omega_{i,1}\tilde{s}_{i,21} - c_{i,1}s_{i,21} - \mu_{i,1}\beta_{i,1} \\ & - \frac{1}{\iota_{i,1}}\tilde{\alpha}_{i,1} - \hat{\chi}_{i,1}\tanh\left(\frac{\hat{\chi}_{i,1}\tilde{\alpha}_{i,1}}{\sigma_{i,1}}\right) - \hat{D}_{i,1} + 2f_{i,1}],\end{aligned} \tag{91}$$

and

$$\begin{aligned}\tau_{i,r} = {} & b_{i,3}^{-1}[-\hat{\vartheta}_{i,3}\Omega_{i,3}\tilde{s}_{i,23} - c_{i,3}s_{i,23} - \mu_{i,3}\beta_{i,3} \\ & - \frac{1}{\iota_{i,3}}\tilde{\alpha}_{i,3} - \hat{\chi}_{i,3}\tanh\left(\frac{\hat{\chi}_{i,3}\tilde{\alpha}_{i,3}}{\sigma_{i,3}}\right) - \hat{D}_{i,3} - 2b_i s_{i,13}].\end{aligned} \tag{92}$$

3. Results

3.1. Stability Analysis

Theorem 1. *Consider the multi-USV system* (16) *and* (17) *under the pose-measurement FDI attack* (18)*. Suppose that Assumptions 1–4 hold and that the initial condition satisfies* $|z_{ij}^s(t_0)| < \kappa_{ij}^s\rho_i(t_0)$ *for all* $(i,j) \in \mathcal{E}$*. If the tightened boundary condition* (66) *is satisfied and the controller* (70)–(92) *is applied, then all closed-loop signals are uniformly ultimately bounded. Moreover, the transformed error domain* (48) *is not violated, and the true inter-USV distance satisfies*

$$l_{ij,\mathrm{col}} < l_{ij}(t) < l_{ij,\mathrm{con}}, \qquad t \geq t_0.$$

Proof. Following standard Lyapunov and adaptive backstepping arguments [28–30], let

$$V_{i,1} = \frac{1}{2}(s_{i,11}^2 + s_{i,12}^2 + s_{i,13}^2), \tag{93}$$

and

$$V_{i,2} = \frac{1}{2}\sum_{q=1}^{3}\left(\hat{s}_{i,2q}^2 + \tilde{s}_{i,2q}^2 + \tilde{D}_{i,q}^2 + \Gamma_{i,q}^{-1}\tilde{\vartheta}_{i,q}^2\right), \tag{94}$$

where

$$\tilde{D}_{i,q} = \hat{D}_{i,q} - D_{i,q}, \qquad \tilde{\vartheta}_{i,q} = \vartheta_{i,q} - \hat{\vartheta}_{i,q}. \tag{95}$$

Define

$$\tilde{\chi}_{i,q} = \hat{\chi}_{i,q} - \chi_{i,q}, \tag{96}$$

where $\chi_{i,q} > 0$ is a finite constant satisfying

$$|\dot{\alpha}_{i,q} + f_{i,q}| \le \chi_{i,q}, \quad q = 1, 2, \tag{97}$$

and

$$|\dot{\alpha}_{i,3} - b_i s_{i,13}| \le \chi_{i,3} \tag{98}$$

on the compact operating set. Choose the Lyapunov function

$$V = \sum_{i=1}^{N} (V_{i,1} + V_{i,2}) + \frac{1}{2} \sum_{i=1}^{N} \sum_{q=1}^{3} \left(\tilde{\alpha}_{i,q}^2 + \iota_{i,q}^{-1} \tilde{\chi}_{i,q}^2 \right). \tag{99}$$

First, using (55) and (60), one obtains

$$\begin{aligned} \dot{V}_{i,1} = {} & S_{i,1}^T (-H_{i,1}^s X_i + H_{i,2}^s - D_i^s + \Delta_i^a) \\ & + s_{i,13} (b_i r_i - \varpi_i^s + \Delta_{i,\psi}^a). \end{aligned} \tag{100}$$

From (75),

$$X_i = S_{i,2} + \bar{\alpha}_i + \bar{\beta}_i = S_{i,2} + \alpha_i + \tilde{\alpha}_i + \bar{\beta}_i, \tag{101}$$

where $\bar{\beta}_i = [\tanh(\beta_{i,1}), \tanh(\beta_{i,2})]^T$. Moreover,

$$r_i = s_{i,23} + \alpha_{i,3} + \tilde{\alpha}_{i,3} + \tanh(\beta_{i,3}). \tag{102}$$

Substituting (70) and (71) into (100) gives

$$\begin{aligned} \dot{V}_{i,1} = {} & -S_{i,1}^T K_{i,1} S_{i,1} - f_i^T (S_{i,2} + \tilde{\alpha}_i) - f_i^T \bar{\beta}_i - f_i^T \Theta_i \\ & - k_{i,13} s_{i,13}^2 + b_i s_{i,13} (s_{i,23} + \tilde{\alpha}_{i,3}) + b_i s_{i,13} \tanh(\beta_{i,3}) \\ & - b_i s_{i,13} \Theta_{i,3} + S_{i,1}^T \Delta_i^a + s_{i,13} \Delta_{i,\psi}^a. \end{aligned} \tag{103}$$

By Lemma 2,

$$-f_i^T \Theta_i \le \kappa_{\tanh} (\bar{\sigma}_{i,1} + \bar{\sigma}_{i,2}), \tag{104}$$

and

$$-b_i s_{i,13} \Theta_{i,3} \le \kappa_{\tanh} \bar{\sigma}_{i,3}. \tag{105}$$

Since $\|\bar{\beta}_i\| \le \sqrt{2}$ and $|\tanh(\beta_{i,3})| \le 1$, for any $\varepsilon_{\beta,i} > 0$,

$$-f_i^T \bar{\beta}_i \le \frac{\varepsilon_{\beta,i}}{2} \|S_{i,1}\|^2 + \frac{\bar{H}_i^2}{\varepsilon_{\beta,i}}, \tag{106}$$

and

$$b_i s_{i,13} \tanh(\beta_{i,3}) \le \frac{\varepsilon_{\beta,i}}{2} s_{i,13}^2 + \frac{b_i^2}{2\varepsilon_{\beta,i}}. \tag{107}$$

Furthermore, because Δ_i^a and $\Delta_{i,\psi}^a$ are bounded, for any $\varepsilon_{a,i} > 0$,

$$S_{i,1}^T \Delta_i^a + s_{i,13} \Delta_{i,\psi}^a \le \frac{\varepsilon_{a,i}}{2} \|s_{i,1}\|^2 + \frac{\bar{\Delta}_{a,i}^2}{2\varepsilon_{a,i}}, \tag{108}$$

where $s_{i,1} = [S_{i,1}^T, s_{i,13}]^T$ and $\bar{\Delta}_{a,i}$ is a finite residual bound. Therefore,

$$\begin{aligned} \dot{V}_{i,1} \le {} & -\left(\lambda_{\min}(K_{i,1}) - \frac{\varepsilon_{a,i} + \varepsilon_{\beta,i}}{2} \right) \|S_{i,1}\|^2 \\ & - \left(k_{i,13} - \frac{\varepsilon_{a,i} + \varepsilon_{\beta,i}}{2} \right) s_{i,13}^2 \\ & - f_i^T (S_{i,2} + \tilde{\alpha}_i) + b_i s_{i,13} (s_{i,23} + \tilde{\alpha}_{i,3}) \\ & + M_{i,1}, \end{aligned} \tag{109}$$

where $M_{i,1} > 0$ collects the finite constants generated by the tanh bounds, saturation auxiliary bounds, and attack

residual bounds.

Second, differentiating $s_{i,2q}$ in (75) and using (17) and (72) yield

$$\begin{aligned}\dot{s}_{i,21} = {} & \theta_{i,1}^{*T}\varphi_{i,1} + D_{i,1} + b_{i,1}\,\mathrm{sat}(\tau_{i,u}) + \frac{1}{\iota_{i,1}}\tilde{\alpha}_{i,1} \\ & - \mathrm{sech}^2(\beta_{i,1})\dot{\beta}_{i,1} + \hat{\chi}_{i,1}\tanh\left(\frac{\hat{\chi}_{i,1}\tilde{\alpha}_{i,1}}{\sigma_{i,1}}\right),\end{aligned} \tag{110}$$

$$\begin{aligned}\dot{s}_{i,22} = {} & \theta_{i,2}^{*T}\varphi_{i,2} + D_{i,2} + \frac{1}{\iota_{i,2}}\tilde{\alpha}_{i,2} - \mathrm{sech}^2(\beta_{i,2})\dot{\beta}_{i,2} \\ & + \hat{\chi}_{i,2}\tanh\left(\frac{\hat{\chi}_{i,2}\tilde{\alpha}_{i,2}}{\sigma_{i,2}}\right),\end{aligned} \tag{111}$$

and

$$\begin{aligned}\dot{s}_{i,23} = {} & \theta_{i,3}^{*T}\varphi_{i,3} + D_{i,3} + b_{i,3}\,\mathrm{sat}(\tau_{i,r}) + \frac{1}{\iota_{i,3}}\tilde{\alpha}_{i,3} \\ & - \mathrm{sech}^2(\beta_{i,3})\dot{\beta}_{i,3} + \hat{\chi}_{i,3}\tanh\left(\frac{\hat{\chi}_{i,3}\tilde{\alpha}_{i,3}}{\sigma_{i,3}}\right).\end{aligned} \tag{112}$$

Using (80)–(86) and $\tilde{D}_{i,q} = \hat{D}_{i,q} - D_{i,q}$, the derivative of $V_{i,2}$ can be arranged as

$$\begin{aligned}\dot{V}_{i,2} = \sum_{q=1}^{3}\Big[& - c_{i,q}\hat{s}_{i,2q}^2 - c_{i,eq}\hat{s}_{i,2q}\tilde{s}_{i,2q} \\ & - (c_{i,q} + c_{i,eq})\tilde{s}_{i,2q}^2 - \tilde{s}_{i,2q}\theta_{i,q}^{*T}\varphi_{i,q} \\ & + \hat{\vartheta}_{i,q}\Omega_{i,q}\tilde{s}_{i,2q}^2 - c_{i,dq}(c_{i,Dq} - 1)\tilde{D}_{i,q}\hat{D}_{i,q} \\ & - \tilde{D}_{i,q}\dot{D}_{i,q} + \Gamma_{i,q}^{-1}\tilde{\vartheta}_{i,q}\dot{\hat{\vartheta}}_{i,q}\Big] \\ & + s_{i,21}f_{i,1} + s_{i,22}f_{i,2} - b_i s_{i,23}s_{i,13}.\end{aligned} \tag{113}$$

From the definition of $\Omega_{i,q}$,

$$-\tilde{s}_{i,2q}\theta_{i,q}^{*T}\varphi_{i,q} \le -\vartheta_{i,q}\Omega_{i,q}\tilde{s}_{i,2q}^2 + \gamma_{i,q}^2. \tag{114}$$

Together with the adaptive law (87), the terms containing $\tilde{\vartheta}_{i,q}\Omega_{i,q}\tilde{s}_{i,2q}^2$ are canceled. Applying Young's inequality to the remaining cross terms gives

$$\begin{aligned}\dot{V}_{i,2} \le \sum_{q=1}^{3}\Big[& - \left(c_{i,q} - \frac{c_{i,eq}}{2}\right)\hat{s}_{i,2q}^2 - \left(c_{i,q} + \frac{c_{i,eq}}{2}\right)\tilde{s}_{i,2q}^2 \\ & - \frac{c_{i,dq}(c_{i,Dq} - 1) - 1}{2}\tilde{D}_{i,q}^2 - \frac{\lambda_{i,q}}{2}\tilde{\vartheta}_{i,q}^2 \\ & + \frac{\lambda_{i,q}}{2}\vartheta_{i,q}^2 + \frac{c_{i,dq}(c_{i,Dq} - 1)}{2}D_{i,q}^{*2} + \frac{1}{2}\bar{D}_{i,q}^2 + \gamma_{i,q}^2\Big] \\ & + s_{i,21}f_{i,1} + s_{i,22}f_{i,2} - b_i s_{i,23}s_{i,13},\end{aligned} \tag{115}$$

where $D_{i,q}^*$ and $\bar{D}_{i,q}$ are finite bounds of $D_{i,q}$ and $\dot{D}_{i,q}$, respectively.

Third, differentiating the filter-error and $\hat{\chi}_{i,q}$-error terms in (99), and using (72) and (74), gives

$$\begin{aligned}\dot{V}_{\alpha\chi,i} = \sum_{q=1}^{3}\Bigg[& -\frac{1}{\iota_{i,q}}\tilde{\alpha}_{i,q}^2 - \hat{\chi}_{i,q}\tilde{\alpha}_{i,q}\tanh\left(\frac{\hat{\chi}_{i,q}\tilde{\alpha}_{i,q}}{\sigma_{i,q}}\right) \\ & -\tilde{\alpha}_{i,q}\dot{\alpha}_{i,q} + \tilde{\chi}_{i,q}|\tilde{\alpha}_{i,q}| - \frac{\ell_{i,q}}{\iota_{i,q}}\tilde{\chi}_{i,q}\hat{\chi}_{i,q}\Bigg].\end{aligned} \tag{116}$$

When (109), (115), and (116) are combined, the remaining filter-error coupling terms satisfy

$$-\tilde{\alpha}_{i,q}(\dot{\alpha}_{i,q} + f_{i,q}) \le \chi_{i,q}|\tilde{\alpha}_{i,q}|, \qquad q = 1, 2, \tag{117}$$

and

$$-\tilde{\alpha}_{i,3}(\dot{\alpha}_{i,3} - b_i s_{i,13}) \le \chi_{i,3}|\tilde{\alpha}_{i,3}|. \tag{118}$$

Hence, by Lemma 2 and Young's inequality,

$$\begin{aligned}\dot{V}_{\alpha\chi,i} \le \sum_{q=1}^{3}\Big[&- \iota_{i,q}^{-1}\tilde{\alpha}_{i,q}^2 - \frac{\ell_{i,q}}{2\iota_{i,q}}\tilde{\chi}_{i,q}^2 \\ &+ \frac{\ell_{i,q}}{2\iota_{i,q}}\chi_{i,q}^2 + \kappa_{\tanh}\sigma_{i,q}\Big].\end{aligned} \tag{119}$$

Combining (109), (115), and (119), the coupling terms $s_{i,21}f_{i,1}$, $s_{i,22}f_{i,2}$, and $b_i s_{i,23}s_{i,13}$ are canceled. Thus, there exist positive constants C and M such that

$$\dot{V} \le -CV + M, \tag{120}$$

provided that the design parameters satisfy

$$\begin{aligned}&\lambda_{\min}(K_{i,1}) > \frac{\varepsilon_{a,i} + \varepsilon_{\beta,i}}{2}, \quad k_{i,13} > \frac{\varepsilon_{a,i} + \varepsilon_{\beta,i}}{2}, \\ &c_{i,q} > \frac{c_{i,eq}}{2}, \quad c_{i,dq}(c_{i,Dq} - 1) > 1, \quad \lambda_{i,q} > 0, \quad \ell_{i,q} > 0.\end{aligned} \tag{121}$$

The constant $M > 0$ contains only finite quantities, including the attack-residual bounds, approximation bounds, disturbance-observer bounds, auxiliary-saturation bounds, and tanh approximation constants.

Solving (120) yields

$$V(t) \le \left(V(t_0) - \frac{M}{C}\right) e^{-C(t-t_0)} + \frac{M}{C}. \tag{122}$$

Therefore, all signals included in V are uniformly ultimately bounded. Consequently, $S_{i,1}$, $s_{i,13}$, $\hat{s}_{i,2q}$, $\tilde{s}_{i,2q}$, $\tilde{D}_{i,q}$, $\tilde{\vartheta}_{i,q}$, $\tilde{\alpha}_{i,q}$, and $\tilde{\chi}_{i,q}$ are bounded. From the filter, predictor, observer, and control laws, the remaining closed-loop signals are also bounded. In addition, ξ_{ij}^s is bounded. Since $\xi_{ij}^s \to \pm\infty$ as $z_{ij}^s \to \pm\kappa_{ij}^s\rho_i$, the domain (48) is not violated. Hence,

$$l_{ij,d} - \kappa_{ij}^s\rho_i(t) < l_{ij}^s(t) < l_{ij,d} + \kappa_{ij}^s\rho_i(t). \tag{123}$$

Using $0 < \rho_i(t) \le 1$, (64), and (66), the true distance satisfies

$$l_{ij}(t) > l_{ij,d} - \kappa_{ij}^s - \bar{\delta}_{ij} > l_{ij,\mathrm{col}}, \tag{124}$$

and

$$l_{ij}(t) < l_{ij,d} + \kappa_{ij}^s + \bar{\delta}_{ij} < l_{ij,\mathrm{con}}. \tag{125}$$

This completes the proof. □

Corollary 1. *If the attack-estimation residual is zero, i.e., $n_i \equiv 0$, then $\Delta_i^a = 0$, $\Delta_{i,\psi}^a = 0$, and $\bar{\delta}_{ij} = 0$. In this case, the tightened boundary condition reduces to the nominal prescribed-time formation constraint, and the proposed controller recovers the attack-free distributed prescribed-time formation result.*

Remark 2. *The boundedness conclusion holds under the assumptions, initial-domain condition, tightened-boundary condition, and gain conditions of Theorem 1. The estimate $\dot{V} \le -CV + M$ first establishes boundedness on the maximal solution interval. This prevents finite-time escape and permits continuation of the solution for all $t \ge t_0$, so the states remain in a compact Lyapunov sublevel set rather than being assumed bounded a priori. If an initial transformed error lies outside its admissible domain, $H_{i,1}^s$ approaches singularity, an attack exceeds the assumed magnitude or rate bounds, or the gain and tightened-boundary conditions are violated, the theorem no longer guarantees boundedness. In such a case, the transformed error can approach its singular boundary, the neural approximation can leave its valid compact domain, and collision avoidance or connectivity maintenance can be lost.*

3.2. Simulation Analysis

Numerical simulations are presented to verify the proposed secure-pose prescribed-time formation controller. The formation consists of one virtual leader, denoted by USV0, and four follower USVs, denoted by USV1–USV4.

The directed communication graph is shown in Figure 1. USV1 and USV2 receive the information from USV0, USV3 receives the information from USV1, and USV4 receives the information from USV2. The desired relative displacements are selected as $[6,-3]^T$, $[6,3]^T$, $[6,0]^T$ and $[6,0]^T$, respectively. Thus, the desired distances of the four formation edges are $\sqrt{45}$ m, $\sqrt{45}$ m, 6 m and 6 m.

The reference trajectory generated by USV0 is given by $x_0(t) = 0.55t$ and $y_0(t) = 4\sin(0.035t)$, and the heading angle is obtained from the tangent direction of the reference path. The initial poses of USV1–USV4 are chosen as $[-7.4, 2.5, 0.18]^T$, $[-5.9, -5.1, 0.05]^T$, $[-13.0, 0.8, 0.12]^T$, and $[-11.7, -6.5, -0.02]^T$, respectively. The initial velocities of the followers are set to zero.

The model parameters are $m_{11} = 25$, $m_{22} = 30$, $I_z = 8$, $X_u = 2.0$, $X_{uu} = 2.2$, $Y_v = 1.0$, $Y_{vv} = 1.6$, $N_r = 1.3$, and $N_{rr} = 1.1$. The surge and yaw input saturation levels are $[-35, 65]$ N and $[-18, 18]$ N m, respectively. The bounded disturbances are implemented as

$$\begin{aligned} d_{i,u}(t) &= A_{i,u}\sin(\omega_{i,u}t + \phi_{i,u}), \\ d_{i,v}(t) &= A_{i,v}\cos(\omega_{i,v}t + \phi_{i,v}), \\ d_{i,r}(t) &= A_{i,r}\sin(\omega_{i,r}t + \phi_{i,r}), \end{aligned} \tag{126}$$

where the amplitudes, frequencies, and phases are listed in Table 1.

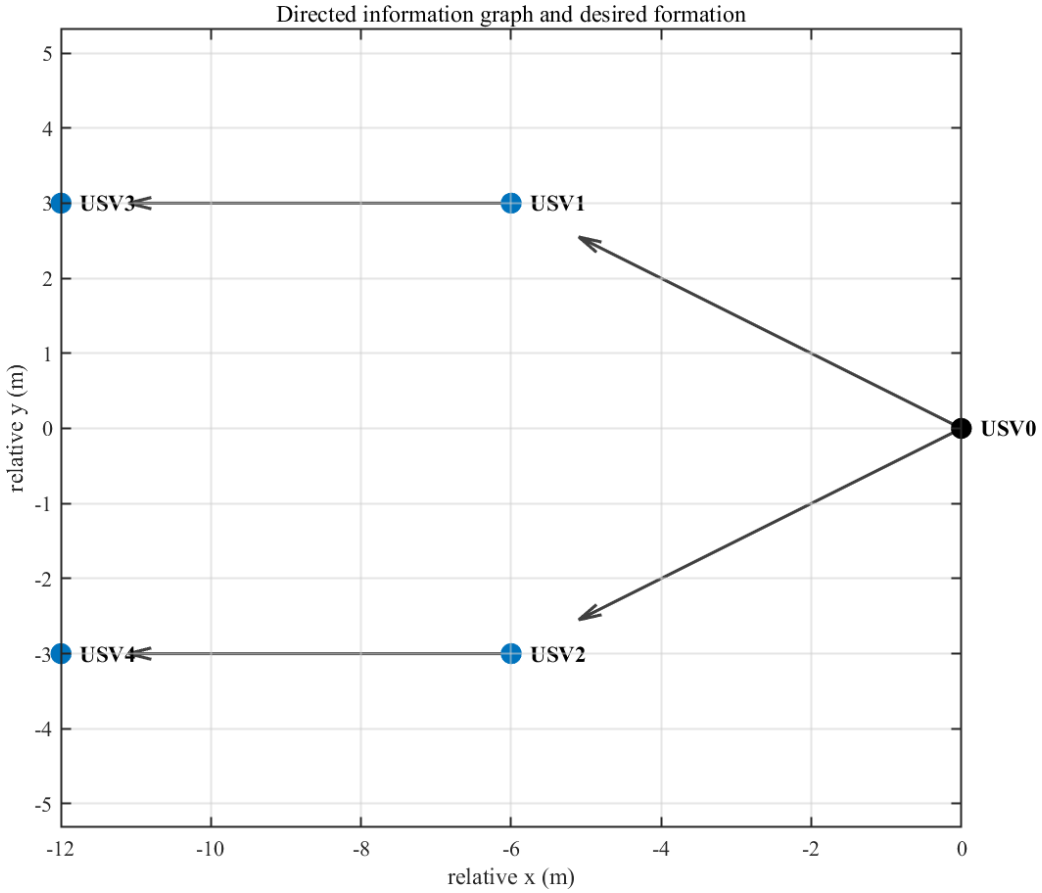


Figure 1. Directed communication graph and desired formation.

The prescribed-time parameters are selected uniformly as $T_i = T_p = 25$ s, $\rho_{i,0} = \rho_0 = 1.0$, and $\rho_{i,\infty} = \rho_\infty = 0.18$. The tightened prescribed-performance boundary parameters are $\kappa^s_{10} = 3.2$, $\kappa^s_{20} = 3.2$, $\kappa^s_{31} = 2.8$, and $\kappa^s_{42} = 2.8$. The collision-avoidance distance and the maximum communication distance are set as 2 m and 12 m, respectively. The controller gains are $k_p = 0.62$, $k_\xi = 0.42$, $k_\theta = 0.28$, $k_{\mathrm{h}} = 1.85$, $k_u = 2.70$, $k_r = 2.45$, and $k_\psi = 1.05$.

The pose-measurement FDI attacks are injected into the transmitted pose information of USV1–USV4. To make the numerical experiment consistent with Assumption 3, both the attack onset at $t_a = 35$ s and the additional pulse over 55–75 s are generated by continuously differentiable transitions. Define

$$S_\varepsilon(t;t_0)=\begin{cases}0, & t\le t_0-\varepsilon/2,\\ 3r^2-2r^3, & t_0-\varepsilon/2<t<t_0+\varepsilon/2,\\ 1, & t\ge t_0+\varepsilon/2,\end{cases}\qquad r=\frac{t-(t_0-\varepsilon/2)}{\varepsilon},$$

and set

$$g_a(t)=S_\varepsilon(t;35),\qquad \chi_{p,\varepsilon}(t)=S_\varepsilon(t;55)-S_\varepsilon(t;75),\quad \varepsilon=\varepsilon_s>0.$$

The transition width is selected as $\varepsilon_s=1.0$ s. For $i=1,\dots,4$, let $\varphi_i=0.65i$. The unsaturated attack components are selected as

$$\begin{aligned}a_{xi}(t)&=g_a(t)(1.10+0.32i)\sin\big(0.105(t-t_a)+\varphi_i\big)\\&\quad+\chi_{p,\varepsilon}(t)(0.65+0.10i),\\ a_{yi}(t)&=g_a(t)(0.92+0.24i)\cos\big(0.085(t-t_a)+0.8\varphi_i\big)\\&\quad-\chi_{p,\varepsilon}(t)(0.48+0.07i),\\ a_{\psi i}(t)&=g_a(t)(0.105+0.014i)\sin\big(0.165(t-t_a)+0.45\varphi_i\big).\end{aligned}$$

The final attack is obtained with the smooth componentwise saturation

$$a_i(t)=\bar a\odot\tanh\big([a_{xi}(t),a_{yi}(t),a_{\psi i}(t)]^T\oslash\bar a\big),\qquad \bar a=[4.5,4.5,0.55]^T,$$

where $\odot$ and $\oslash$ denote componentwise multiplication and division. This construction makes a_i and $\dot a_i$ continuous and bounded. Three cases are compared: the nominal case without attack, the uncompensated pose-measurement-FDI case, and the proposed secure-pose compensation case.

For the four formation edges, Equation (66) can be checked explicitly. The virtual leader is attack free, so $\bar n_{p,0}=0$. For edges $(1,0)$ and $(2,0)$, the available geometric margin is

$$\min\{\sqrt{45}-2,12-\sqrt{45}\}=4.7082\ \text{m},$$

and $\kappa^s_{ij}=3.2$ requires $\bar\delta_{ij}<1.5082$ m. For edges $(3,1)$ and $(4,2)$, the available margin is $\min\{6-2,12-6\}=4$ m, and $\kappa^s_{ij}=2.8$ requires $\bar\delta_{ij}<1.2$ m. The observed maximum edge residuals were 0.1725, 0.2465, 0.2728, and 0.2602 m. Conservative reported bounds of 0.20, 0.28, 0.32, and 0.30 m, respectively, are used in Table 2; all four satisfy Equation (66).

Table 2. Edgewise numerical verification of the tightened-boundary condition.

Edge	$l_{ij,d}$	κ^s_{ij}	$\bar\delta_{ij}$	Right-Hand Side	Required Check
$(1,0)$	6.7082	3.2	0.20	4.7082	satisfied
$(2,0)$	6.7082	3.2	0.28	4.7082	satisfied
$(3,1)$	6.0000	2.8	0.32	4.0000	satisfied
$(4,2)$	6.0000	2.8	0.30	4.0000	satisfied

For clarity, the reported performance indices are defined over the edge set $\mathcal{E}_f=\{(1,0),(2,0),(3,1),(4,2)\}$, with $N_e=4$, simulation interval $[t_1,t_2]=[0,120]$ s, and final window $T_f=10$ s. Let $e^l_{ij}(t)=l_{ij}(t)-l_{ij,d}$. The mean absolute distance error, maximum absolute distance error, and final-window RMS distance error are

$$E_{\text{mean}}=\frac{1}{N_e(t_2-t_1)}\sum_{(i,j)\in\mathcal{E}_f}\int_{t_1}^{t_2}|e^l_{ij}(t)|\,dt, \tag{127}$$

$$E_{\max}=\max_{(i,j)\in\mathcal{E}_f,\,t\in[t_1,t_2]}|e^l_{ij}(t)|, \tag{128}$$

$$E_{\text{RMS,final}}=\sqrt{\frac{1}{N_eT_f}\sum_{(i,j)\in\mathcal{E}_f}\int_{t_2-T_f}^{t_2}[e^l_{ij}(t)]^2\,dt}. \tag{129}$$

Because position and yaw have different physical units, their attack-estimation errors are reported separately:

$$E_{a,p} = \sqrt{\frac{1}{2N_f(t_2 - t_a)} \sum_{i=1}^{N_f} \int_{t_a}^{t_2} \left[(a_{x,i} - \hat{a}_{x,i})^2 + (a_{y,i} - \hat{a}_{y,i})^2\right] dt}, \tag{130}$$

$$E_{a,\psi} = \sqrt{\frac{1}{N_f(t_2 - t_a)} \sum_{i=1}^{N_f} \int_{t_a}^{t_2} (a_{\psi,i} - \hat{a}_{\psi,i})^2 dt}. \tag{131}$$

For the uncompensated case, no estimator is present and $\hat{a}_i \equiv 0$ is used only to define a zero-estimate baseline; it is not described as estimator performance.

The numerical simulation results are shown in Figures 1–9. The proposed estimator tracks all three attack components closely after a short transient, and the true distances remain inside the collision-avoidance and connectivity limits. Figure 8 further shows that every edgewise pose-reconstruction residual remains below its available safety margin. The gray bands and vertical lines in the time-domain figures identify the smooth pulse interval, prescribed time, and attack onset, respectively.

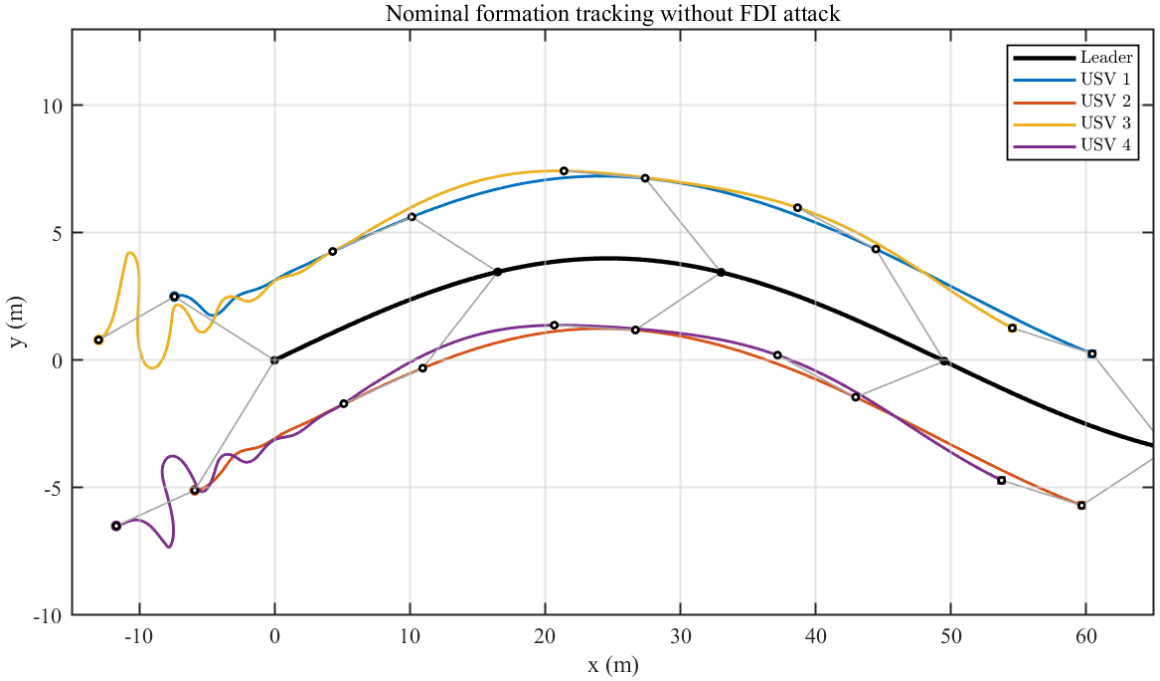


Figure 2. Trajectories of formation tracking without pose-measurement FDI attacks.

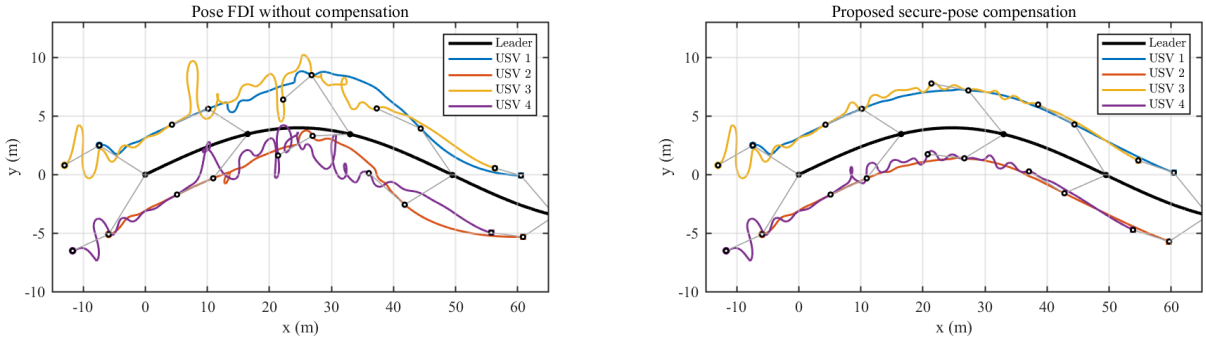


Figure 3. Trajectory comparison under pose-measurement FDI attacks.

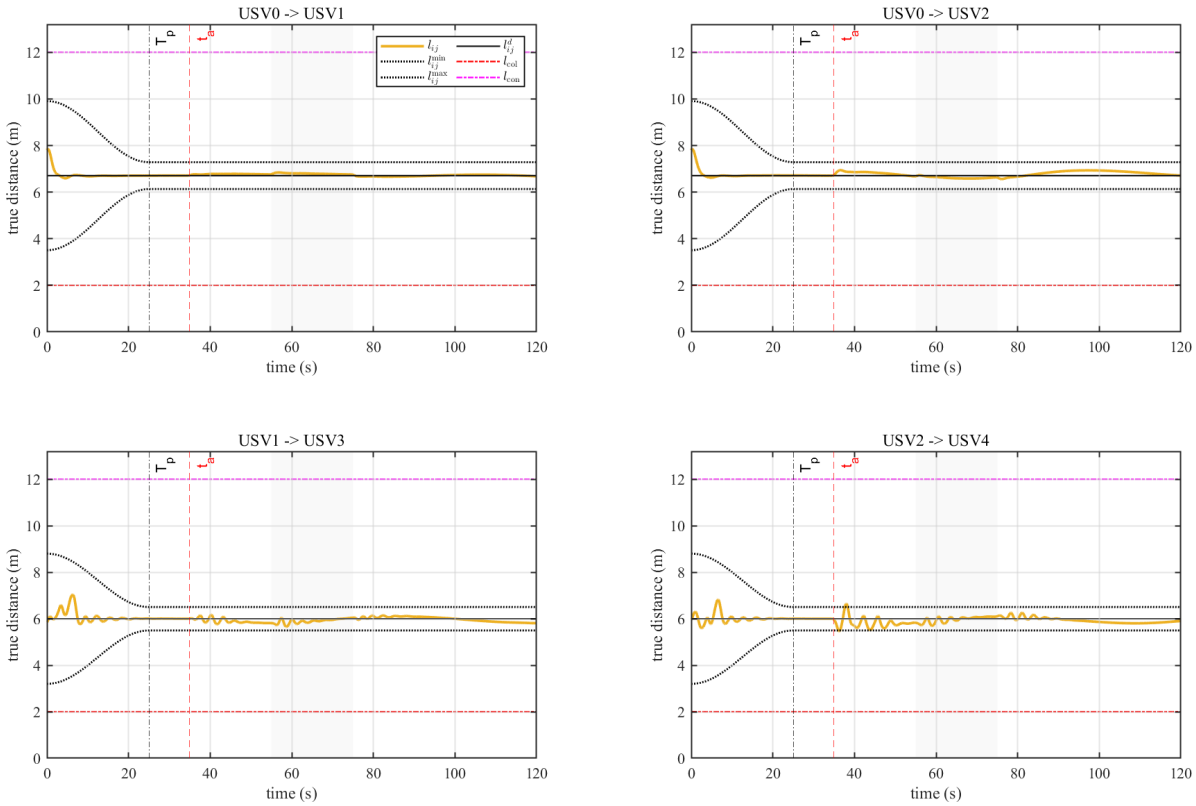


Figure 4. Trajectories of relative distances.

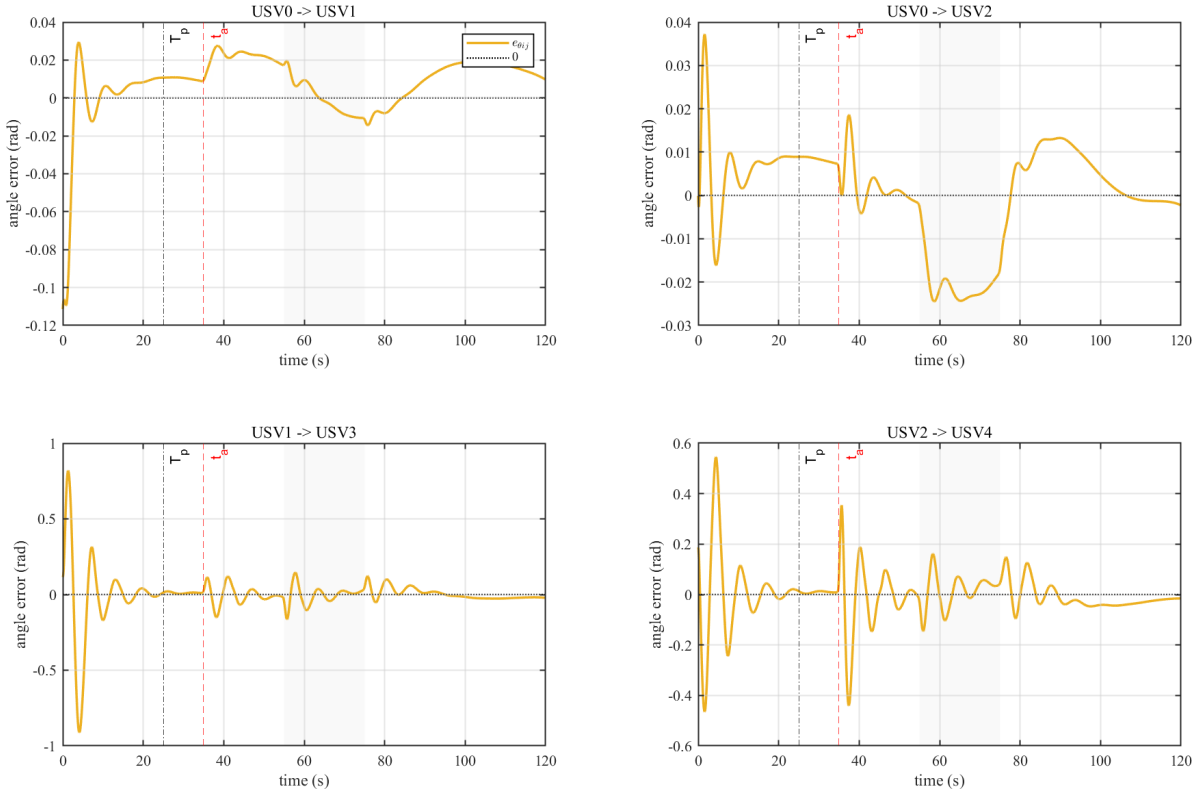


Figure 5. Trajectories of relative angle errors.

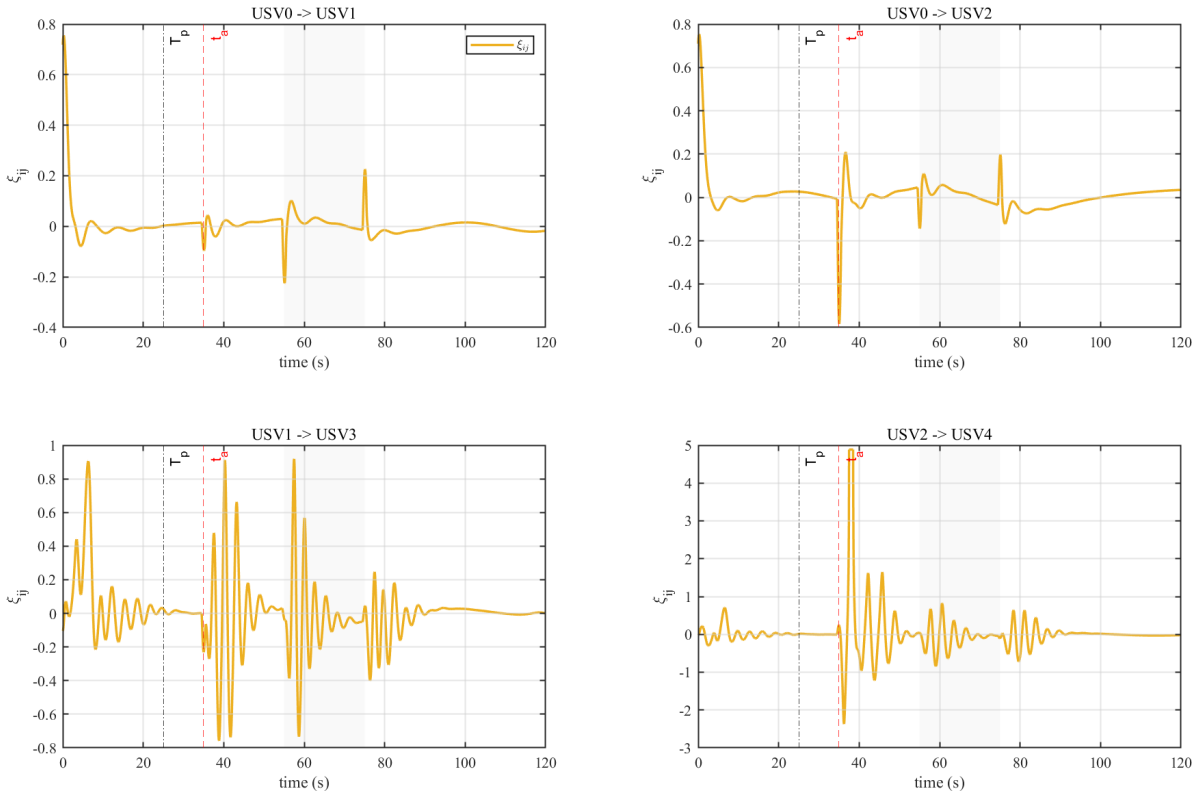


Figure 6. Transformed prescribed-time distance errors.

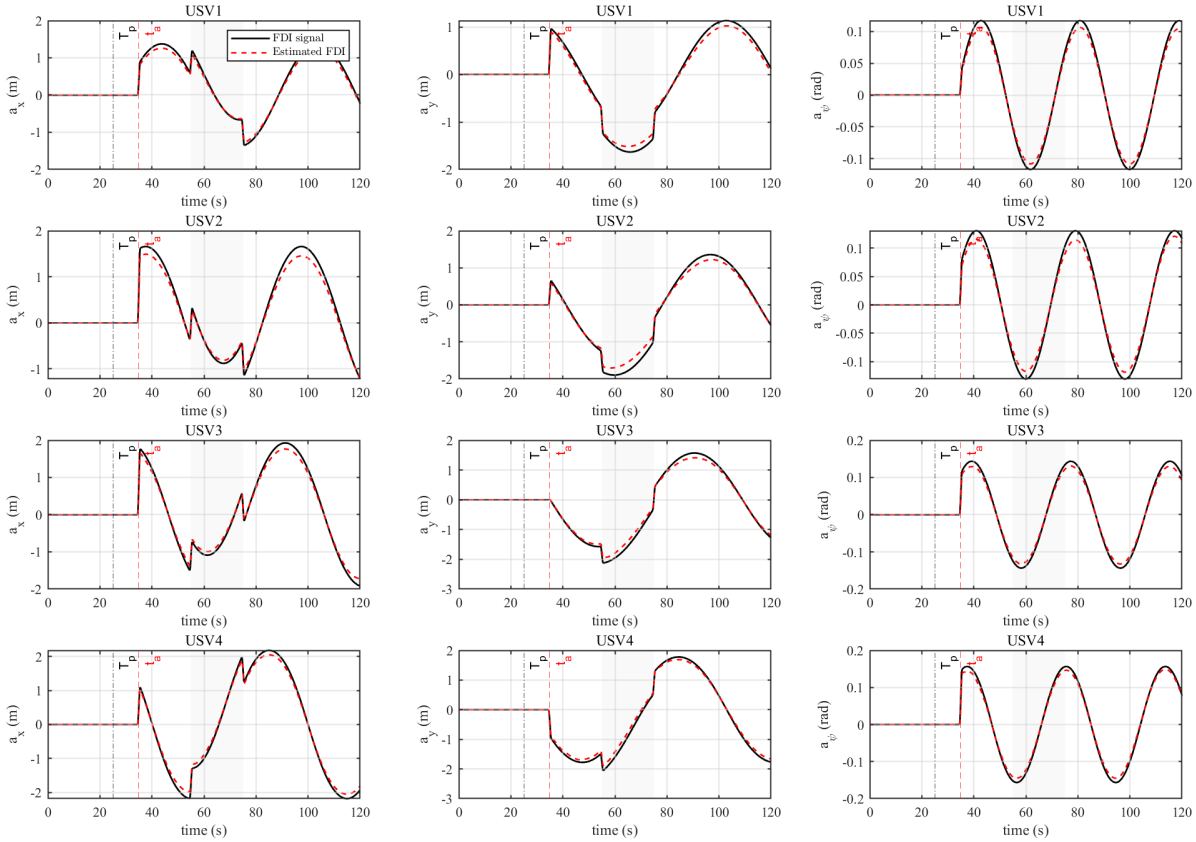


Figure 7. Actual and estimated pose-measurement FDI signals for all four USVs.

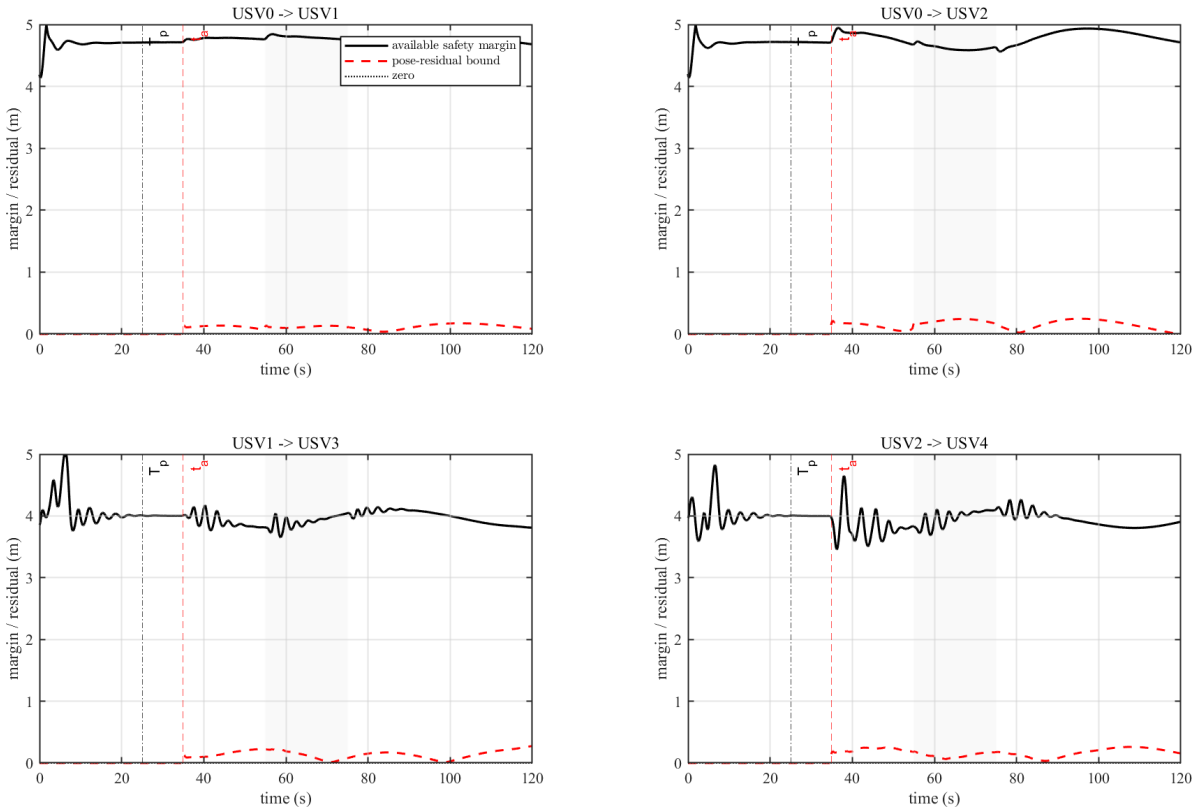


Figure 8. Available true-distance safety margins and edgewise pose-reconstruction residuals.

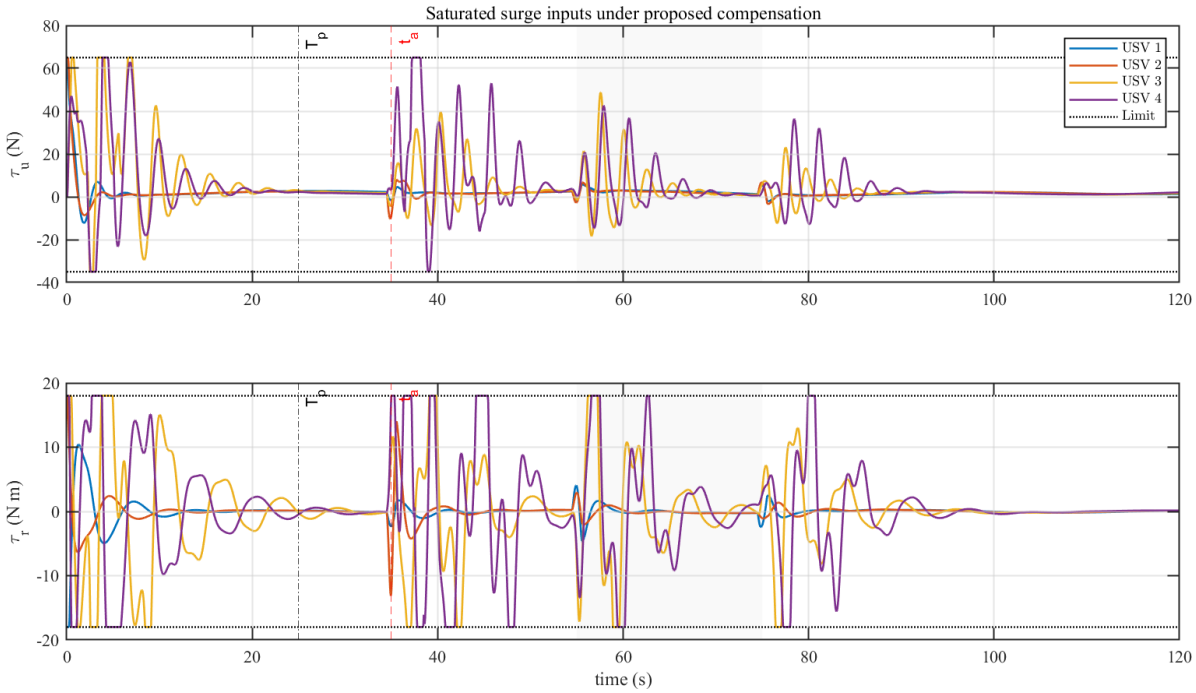


Figure 9. Trajectories of saturated control inputs with the reviewer-requested temporal markers.

The reviewer-requested performance indices obtained from the revised smooth-attack simulation are summarized in Table 3.

Table 3. Comparison of formation and attack-estimation performance.

Case	E_{mean}	$E_{\max}$	$E_{\mathrm{RMS,final}}$	$E_{a,p}$	$E_{a,\psi}$	$l_{\min}$
Attack free	0.0247	1.1542	0.0044	–	–	5.5906
Uncompensated	0.7691	2.9823	1.2807	1.1732	0.1006	3.0177
Proposed	0.0948	1.1542	0.1200	0.1015	0.0087	5.4578

Compared with the uncompensated case, the proposed method reduces the final-window distance RMS from 1.2807 m to 0.1200 m, the position-attack RMSE from 1.1732 m to 0.1015 m, and the yaw-attack RMSE from 0.1006 rad to 0.0087 rad. The minimum true distance remains 5.4578 m, safely above the 2 m collision limit.

4. Discussion

The theoretical and numerical results show that introducing secure-pose reconstruction before the formation-error generation is essential when pose measurements are corrupted by FDI attacks. Compared with a nominal prescribed-time formation controller that directly uses the attacked measurements, the proposed method prevents the injected pose signals from directly distorting the relative-distance and bearing-angle calculations. The tightened performance boundary further converts the bounded pose-reconstruction residual into an explicit safety margin, which explains why the true inter-USV distances can still satisfy the collision-avoidance and connectivity constraints. The method is particularly suitable for networked USV formations in which cooperative control depends on exchanged pose information.

The present validation is limited to numerical simulation. Although the simulations include nonlinear hydrodynamics, disturbances, actuator saturation, and pose-measurement attacks, they do not fully reproduce sensor noise, communication delay and packet loss, actuator dead zones, unmodeled high-frequency dynamics, or real-time computational constraints. Furthermore, Assumption 3 excludes ideal jumps, impulsive attacks, and arbitrarily fast switching attacks. Hardware-in-the-loop tests, model-scale water-tank experiments, and practical multi-USV trials are therefore needed before deployment claims can be made. These tests should quantify noise sensitivity, communication robustness, real-time computational load, and the conservativeness of the residual-dependent safety margins.

5. Conclusions

This paper investigated an attack-resilient distributed prescribed-time formation control problem for underactuated USVs subject to pose-measurement FDI attacks, input saturation, external disturbances, collision-avoidance constraints, and connectivity-maintenance requirements. To prevent corrupted pose measurements from directly entering the formation-error construction, a neural-network-based attack estimator was incorporated to reconstruct secure pose information. Based on the reconstructed pose, a distributed prescribed-time formation controller was developed by combining tightened performance boundaries, logarithmic error transformation, nonlinear filtering, surface-error prediction, predictor-based disturbance observation, saturation compensation, and surge-yaw input design. The residual effect of pose-estimation errors on the relative-distance and bearing-angle dynamics was explicitly characterized, which enabled the prescribed performance boundary to be tightened for the true USV positions. Lyapunov analysis proved that all closed-loop signals are uniformly ultimately bounded, the transformed prescribed-time error remains within its admissible domain, and the actual inter-USV distances satisfy the required collision-free and connectivity-preserving constraints. Simulation results further showed that the proposed secure-pose compensation scheme can reduce the adverse influence of pose-measurement FDI attacks and recover satisfactory formation tracking performance. Future work will focus on hardware-in-the-loop, water-tank, and practical multi-USV experiments, as well as extensions to simultaneous pose-measurement and actuator attacks, nonsmooth or switching attacks, communication delays and packet losses, time-varying communication topologies, and data-driven attack-detection mechanisms.

Author Contributions

X.L.: Conceptualization, methodology, software; X.L.: Data curation, writing—original draft preparation; P.G.: Visualization, investigation; J.L.: Supervision; X.L.: Software, validation; X.L.: Writing—reviewing and editing. All authors have read and agreed to the published version of the manuscript.

Funding

This research received no external funding.

Data Availability Statement

Not applicable.

Acknowledgments

The authors would like to thank the associate editor and reviewers for their very constructive comments and suggestions which will help us to greatly improve the quality and presentation of the paper.

Conflicts of Interest

The authors declare no conflict of interest.

Use of AI and AI-Assisted Technologies

No AI tools were utilized for this paper.

References

1. Fossen, T.I. *Handbook of Marine Craft Hydrodynamics and Motion Control*; Wiley: Chichester, UK, 2011. https://doi.org/10.1002/9781119994138.
2. Pettersen, K.Y.; Nijmeijer, H. Underactuated ship tracking control: Theory and experiments. *Int. J. Control* **2001**, *74*, 1435–1446. https://doi.org/10.1080/00207170110072039.
3. Aguiar, A.P.; Hespanha, J.P. Trajectory-Tracking and Path-Following of Underactuated Autonomous Vehicles with Parametric Modeling Uncertainty. *IEEE Trans. Autom. Control* **2007**, *52*, 1362–1379. https://doi.org/10.1109/tac.2007.902731.
4. Fax, J.A.; Murray, R.M. Information Flow and Cooperative Control of Vehicle Formations. *IEEE Trans. Autom. Control* **2004**, *49*, 1465–1476. https://doi.org/10.1109/tac.2004.834433.
5. Olfati-Saber, R.; Fax, J.A.; Murray, R.M. Consensus and Cooperation in Networked Multi-Agent Systems. *Proc. IEEE* **2007**, *95*, 215–233. https://doi.org/10.1109/jproc.2006.887293.
6. Ren, W.; Beard, R.W.; Atkins, E.M. Information consensus in multivehicle cooperative control. *IEEE Control Syst. Mag.* **2007**, *27*, 71–82. https://doi.org/10.1109/mcs.2007.338264.
7. Wang, Y.; Liu, X.; Wu, Z.; et al. Distributed Prescribed-Time Formation Control for Underactuated Surface Vehicles With Input Saturation: Theory and Experiment. *IEEE Trans. Intell. Transp. Syst.* **2024**, *25*, 18611–18623. https://doi.org/10.1109/tits.2024.3436882.
8. Do, K.D.; Jiang, Z.P.; Pan, J. Global tracking control of underactuated ships with nonzero off-diagonal terms in their system matrices. *Automatica* **2005**, *41*, 87–95. https://doi.org/10.1016/j.automatica.2004.08.005.
9. Bhat, S.P.; Bernstein, D.S. Finite-Time Stability of Continuous Autonomous Systems. *SIAM J. Control Optim.* **2000**, *38*, 751–766. https://doi.org/10.1137/s0363012997321358.
10. Polyakov, A. Nonlinear Feedback Design for Fixed-Time Stabilization of Linear Control Systems. *IEEE Trans. Autom. Control* **2012**, *57*, 2106–2110. https://doi.org/10.1109/tac.2011.2179869.
11. Bechlioulis, C.P.; Rovithakis, G.A. Robust Adaptive Control of Feedback Linearizable MIMO Nonlinear Systems with Prescribed Performance. *IEEE Trans. Autom. Control* **2008**, *53*, 2090–2099. https://doi.org/10.1109/tac.2008.929402.
12. Song, Y.; Wang, Y.; Holloway, J.; et al. Time-varying feedback for regulation of normal-form nonlinear systems in prescribed finite time. *Automatica* **2017**, *83*, 243–251. https://doi.org/10.1016/j.automatica.2017.06.008.
13. Tee, K.P.; Ge, S.S.; Tay, E.H. Barrier Lyapunov Functions for the control of output-constrained nonlinear systems. *Automatica* **2009**, *45*, 918–927. https://doi.org/10.1016/j.automatica.2008.11.017.
14. Liu, Y.; Ning, P.; Reiter, M.K. False data injection attacks against state estimation in electric power grids. In Proceedings of the CCS '09: 16th ACM Conference on Computer and Communications Security 2009, Chicago, IL, USA, 9–13 November 2009; pp. 21–32. https://doi.org/10.1145/1653662.1653666.
15. Mo, Y.; Sinopoli, B. Secure control against replay attacks. In Proceedings of the 2009 47th Annual Allerton Conference on Communication, Control, and Computing (Allerton), Monticello, IL, USA, 30 September–2 October 2009; pp. 911–918. https://doi.org/10.1109/allerton.2009.5394956.
16. Pasqualetti, F.; Dorfler, F.; Bullo, F. Attack Detection and Identification in Cyber-Physical Systems. *IEEE Trans. Autom. Control* **2013**, *58*, 2715–2729. https://doi.org/10.1109/tac.2013.2266831.
17. Fawzi, H.; Tabuada, P.; Diggavi, S. Secure Estimation and Control for Cyber-Physical Systems under Adversarial Attacks. *IEEE Trans. Autom. Control* **2014**, *59*, 1454–1467. https://doi.org/10.1109/tac.2014.2303233.
18. Teixeira, A.; Shames, I.; Sandberg, H.; et al. A secure control framework for resource-limited adversaries. *Automatica* **2015**, *51*, 135–148. https://doi.org/10.1016/j.automatica.2014.10.067.
19. Dibaji, S.M.; Pirani, M.; Flamholz, D.B.; et al. A systems and control perspective of CPS security. *Annu. Rev. Control* **2019**, *47*, 394–411. https://doi.org/10.1016/j.arcontrol.2019.04.011.
20. Sargolzaei, A.; Allen, B.C.; Crane, C.D.; et al. Lyapunov-Based Control of a Nonlinear Multiagent System with a Time-Varying Input Delay Under False-Data-Injection Attacks. *IEEE Trans. Ind. Inform.* **2022**, *18*, 2693–2703. https://doi.org/10.1109/tii.2021.3106009.
21. Ioannou, P.A.; Sun, J. *Robust Adaptive Control*; PTR Prentice-Hall: Upper Saddle River, NJ, USA, 1996.
22. Swaroop, D.; Hedrick, J.K.; Yip, P.P.; et al. Dynamic surface control for a class of nonlinear systems. *IEEE Trans. Autom. Control* **2000**, *45*, 1893–1899. https://doi.org/10.1109/tac.2000.880994.
23. Park, J.; Sandberg, I.W. Universal Approximation Using Radial-Basis-Function Networks. *Neural Comput.* **1991**, *3*, 246–257. https://doi.org/10.1162/neco.1991.3.2.246.
24. Sanner, R.M.; Slotine, J.J.E. Gaussian networks for direct adaptive control. *IEEE Trans. Neural Netw.* **1992**, *3*, 837–863.

https://doi.org/10.1109/72.165588.

25. Polycarpou, M.M. Stable adaptive neural control scheme for nonlinear systems. *IEEE Trans. Autom. Control* **1996**, *41*, 447–451. https://doi.org/10.1109/9.486648.
26. Lewis, F.L.; Jagannathan, S.; Yesildirak, A. *Neural Network Control of Robot Manipulators and Nonlinear Systems*; Taylor & Francis: London, UK, 1999; xxiii, 442p.
27. Chen, W.H.; Yang, J.; Guo, L.; et al. Disturbance-Observer-Based Control and Related Methods—An Overview. *IEEE Trans. Ind. Electron.* **2016**, *63*, 1083–1095. https://doi.org/10.1109/tie.2015.2478397.
28. Dixon, W.E.; Behal, A.; Dawson, D.M.; et al. *Nonlinear Control of Engineering Systems: A Lyapunov-Based Approach*; Birkhäuser Boston: Boston, MA, USA, 2003. https://doi.org/10.1007/978-1-4612-0031-4.
29. Krstic, M.; Kanellakopoulos, I.; Kokotovic, P.V. *Nonlinear and Adaptive Control Design*; Wiley: New York, NY, USA, 1995.
30. Khalil, H.K. *Nonlinear Systems*, 3rd ed.; Prentice Hall: Upper Saddle River, NJ, USA, 2002.